A novel ultra-high strength maraging steel with balanced ductility and creep resistance achieved by nanoscale β-NiAl and Laves phase precipitates [#]

L. Sun[a,*], T.H. Simm[b], T.L. Martin[c], S. McAdam[b], D.R. Galvin [b], K.M. Perkins[b], P.A.J. Bagot[c], M.P. Moody[c], S.W. Ooi[a], P. Hill[d], M.J. Rawson[d], and H.K.D.H. Bhadeshia[a]

a) Department of Materials Science and Metallurgy, University of Cambridge, 27 Charles Babbage Road, Cambridge, CB3 0FS, UK.
b) Institute of Structural Materials, College of Engineering, Swansea University, Swansea SA2 8PP, UK
c) Department of Materials, University of Oxford, Parks Road, Oxford, OX1 3PH, UK.
d) Rolls-Royce plc, P.O. Box 31, Derby, DE24 8BJ, UK
*Corresponding author, Email: L.Sun@cantab.net

Abstract

A novel ultra-high strength precipitation hardened martensitic steel with balanced ductility and creep resistance has been developed. It utilises a unique combination of nanometre scale intermetallic precipitates of Laves phases and β-NiAl to achieve such properties. The mechanical properties of this steel were assessed by tensile and creep testing. With different heat treatments, this steel showed a remarkable combination of mechanical properties: yield strength of >1800 MPa, ultimate tensile strength of ~ 2000 MPa, tensile ductility up to ~8% at room temperature and creep rupture life > 2,000 hours under 700 MPa stress at 500 °C. The microstructures at different length scales were characterised using scanning / transmission electron microscopy and atom probe tomography. The austenisation and ageing temperatures were found be the key factors determining the microstructural development and resulting mechanical properties. Large primary Laves phase precipitates formed at lower austenisation temperatures resulted in reduced creep strength; whilst the small difference (20 °C) in ageing temperatures had significant impact on the spatial distribution characteristics of β-NiAl precipitates. Lower ageing temperature produced much smaller but more uniformly distributed β-NiAl precipitates which contributed to the higher observed yield strength. It is clear from this study that whilst this novel alloy system showed great potentials, careful design of heat treatment is still required to achieve balanced mechanical properties to meet the service requirements in aerospace propulsion systems.

Keywords: Steel, Precipitation, Nanostructure, Transmission electron microscopy (TEM), Atom probe tomography (APT)

---

1. Introduction

Aerospace industries are constantly challenged to improve aircraft fuel efficiency and reduce greenhouse gas emissions driven by economic and environmental factors. For the propulsion systems, such improvements cannot be achieved without the advancement of materials capabilities, e.g. higher strength, better damage tolerance and more importantly higher temperature capability to enable higher operating temperatures and improve the thermal efficiency of the turbine engines [1].

Maraging steels usually consist of a relatively soft and ductile martensitic matrix of very low carbon content strengthened by the precipitation of a large number of nanometre sized intermetallic phases [2, 3]. As a result, this type of steels exhibits an excellent combination of ultrahigh strength with good fracture toughness, and therefore is widely used for critical applications in the aerospace sector since first developed some 40 years ago [4]. Traditional maraging steels such as the 18Ni grades (200, 250, 300, 350 and etc., where the number signifies the yield strength in ksi) contain around 18wt% Ni with high levels of Co (8~13wt.%) and Mo (3~5wt.%) as well as smaller additions of other alloying elements such as Ti and Al [5]. The high Ni content ensures that only martensitic phase transformation occurs during the decomposition of the austenite phase even at moderate to slow cooling rates. However, this also limits the elevated temperature capability of maraging steels, as the martensite enriched with Ni is not thermodynamically stable at elevated temperatures and a reverse transformation to the equilibrium austenite phase can occur after prolonged exposure to high temperatures [6, 7].

In order to provide a material solution for low pressure turbine shaft applications in jet engines, a novel maraging steel with ultra-high strength and good resistance to creep at temperatures up to 500 °C has recently been developed [8, 9]. Unlike the traditional 18Ni maraging steels that mainly utilise Ni_3Ti precipitates to provide strengthening, the new alloy contains much lower amount of Ni (around 7 wt.%). It is strengthened by two nanometre sized intermetallic precipitates, namely an ordered β-NiAl phase which has a B2 (space group *Pm3m*) CsCl superlattice structure and a topological closed packed (TCP) C14 $(Fe,Cr)_2(W,Mo)$ Laves phase (space group *P 6₃/mmc*), to provide the high strength and good creep resistance.

The fine Laves phases precipitates in 9-12% Cr heat resistant steels are recognised to improve creep strength through dispersion hardening and retardation of sub-grain boundaries movement [10-12]. The very fine β-NiAl precipitate, which is coherent with the BCC Fe matrix with a lattice constant of 0.2887 nm at room temperature [13], is utilised in a number of precipitation hardened (PH) martensitic steels such as the widely used PH13-8Mo type steels [14, 15], the

GE1014 steel [16], and more recently a number of new high strength ferritic/martensitic steels under development [17-20]. However, the combination of the Laves phases and β-NiAl precipitates is unique in the novel steel studied in this work. Therefore, it is important to gain better understanding of the structure-property relationship for this novel maraging steel to achieve tailored properties that fit the application requirements.

The aim of the current work is to investigate the effect of heat treatment conditions on the microstructure development and consequently the mechanical properties. Focus is placed on relating the austenisation temperature and ageing temperature to the precipitation behaviour and the resulting tensile strength, ductility and creep life. Microstructures at different length scales were characterised using optical microscopy, scanning electron microscopy (SEM) with electron backscattered diffraction (EBSD), transmission electron microscopy (TEM) and atom probe tomography (APT), whilst the mechanical properties were assessed by tensile and creep tests.

2. Experimental

2.1 The material and heat treatment

The alloy was vacuum induction melted by Tata RD&T, UK Swindon Technology Centre then hot forged to square bars. Subsequently, the forged bars were subjected to a homogenisation heat treatment in vacuum at 1200 °C for 48 hours followed by gas quenching using high purity Argon. The composition of the as-received material is given in Table 1.

Table 1 The chemical composition of the maraging steel

Element	Fe	Cr	Co	Ni	Al	Mo	W
Weight %	68.11	9.90	8.02	6.99	1.80	2.75	2.43
Atomic %	68.76	10.73	7.67	6.71	3.76	1.62	0.75

The calculated equilibrium phase diagram of the steel with this composition using MatCalc software and MC_Fe_2.009 database is given in Figure 1(a). The possible precipitates are identified as B2 β-NiAl and Laves phase. The calculated equilibrium compositions as functions of temperature are given in Figure 1(b) and (c), respectively. Based on the calculated phase diagram, three heat treatment schemes were applied to the as received materials. For heat treatment 1 (HT1), the material was austenitised at 825 °C for 2 hours followed by air quenching, then aged at 560 °C for 5 hours. As can be seen in Figure 1(a), at 825 °C, a certain amount of Laves precipitates should form during austenisation. Heat treatment 2 (HT2) consists of austenisation at 870 °C for 1 hour, air quenching and ageing at 540 °C for 5 hours. For HT3, the

austenisation temperature of 960°C is believed to be high enough to avoid the formation of any precipitates during austenisation. Therefore, all Laves phase precipitates should form during the subsequent ageing heat treatment at 540°C for 5 hours. Conversely, β-NiAl precipitation should only take place during the ageing heat treatment for all three conditions. The heat treatment conditions are summarised in Table 2.
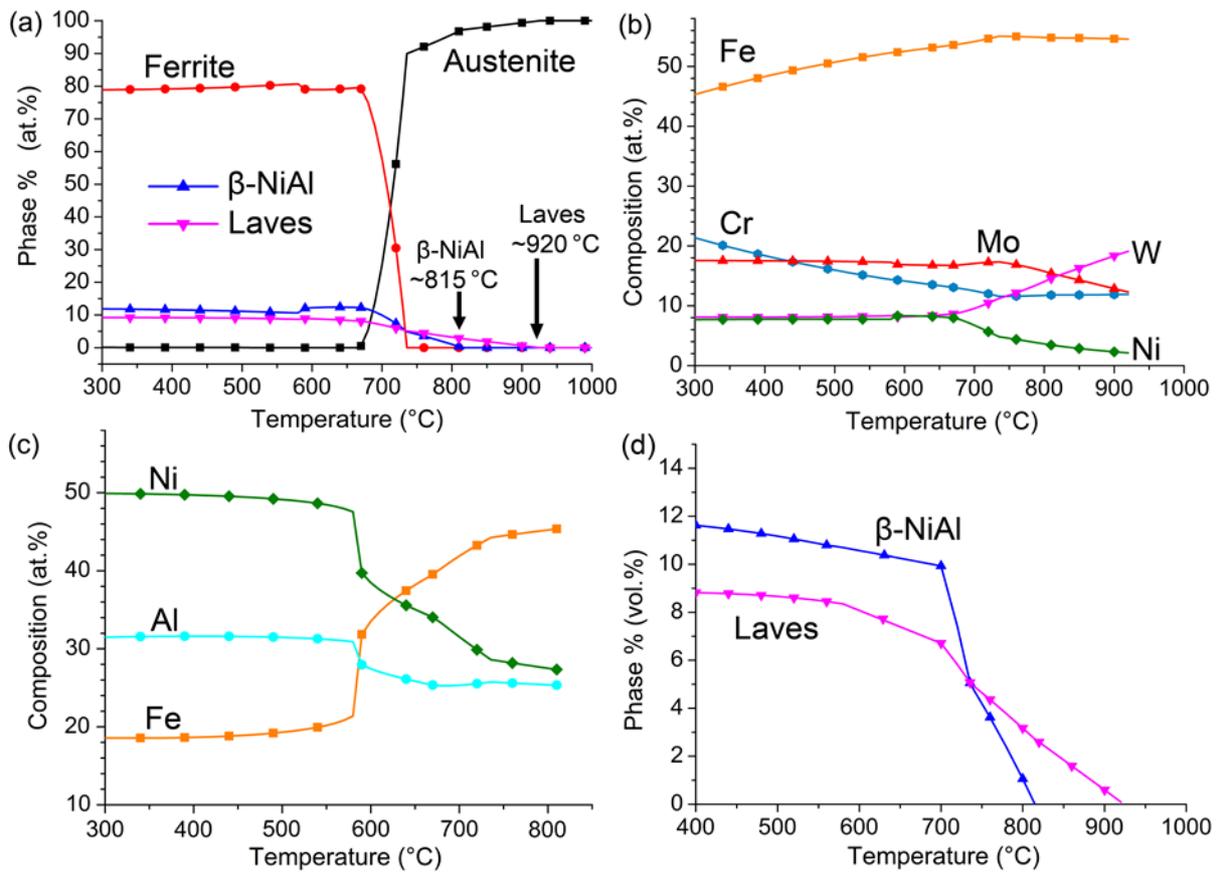
Figure 1 Equilibrium thermodynamics calculation using MatCalc: (a) all phase in at.%, (b) composition of the Laves phase and (c) composition of the β-NiAl as functions of temperature; (d) the calculated volume percentages of Laves phase and β-NiAl.

Similar amounts (in terms of atomic fractions) of Laves phase and β-NiAl are predicted for each heat treatment, based on the calculated phase diagrams. However, as the densities of these two precipitates are quite different, the molar/atomic percentage is not convenient to correlate to microstructural observations and mechanical properties. Therefore, the volume percentages (vol.%) of the two precipitation phases were calculated using the equilibrium density values of β-NiAl and the Laves phase. These values were calculated using the predicted chemical compositions and the ideal structures of the unit cells with lattice parameters of a=0.475 nm and

c=0.773 nm for the Laves phase [21] and a=0.289 nm for β-NiAl [17]. As shown in Figure 1(d), the results suggest that at the ageing temperatures between 540 °C to 560 °C, the equilibrium volumes of the precipitates are around 8-9 vol.% for Laves phase and 10-11 vol.% for β-NiAl.

Table 2 The conditions of heat treatment schemes used in this study

Heat Treatment	Austenisation Temperature (°C)	Austenisation Time (hours)	Ageing Temperature (°C)	Ageing Time (hours)
HT1	825	2	560	5
HT2	870	1	540	5
HT3	960	1	540	5

2.2 Mechanical testing

Following heat treatment, tensile and creep specimens were machined. The specimen designs for both tests were the same, with a gauge diameter of 4 mm and a gauge length of 20 mm. Tensile and creep testing was carried out at SMaRT, Swansea University, Singleton Campus. Tensile tests were conducted with a dual strain-rate of 0.00025 s^{-1} up to 2% strain and 0.068 s^{-1} thereafter, using the standard BS EN ISO 6892. Creep testing was carried out by applying a constant load of 700 MPa to the sample at a temperature of 500 °C following the standard BS EN 10291:2000.

2.3 Optical and electron microscopy

Samples for microstructural observations were prepared for materials in as-austenitised conditions (referred as HT1A, HT2A and HT3A) as well as in conditions after both austenisation and ageing for all three heat treatment schemes (referred as HT1AA, HT2AA and HT3AA, respectively). For optical microscopy, mechanically ground and polished samples were etched using a solution containing 20 ml Nitric acid (60% concentration), 20ml hydrochloric acid (36% concentration) and 60 ml water. For EBSD analysis in SEM, bulk samples were mechanically ground and polished to 1 µm followed by 2 hours of vibratory polishing using colloidal silica with a nominal particle size of 0.04 µm. Thin foil samples for TEM were mechanically thinned then twin jet polished electrochemically using a solution consisting of (by volume) 5% perchloric acid, 25% glycerol and 70% ethanol at 8 °C with a current around 35 mA.

EBSD maps were collected using a FEI Quanta250 SEM operating at 20 kV and an Oxford Instruments HKL Nordlys camera with Channel 5 software. Typical areas of 200 µm by 200 µm

5

were mapped using a step size of 0.25 µm. An indexing rate of at least 80% was achieved, then a post-acquisition noise reduction procedure outlined elsewhere was applied [22].

TEM thin foils were examined using a Philips CM30 TEM with a LaB_6 source operating at 300 kV and a JEOL 2100F FEGTEM operating at 200 kV. TEM images and diffraction patterns were recorded using photographic plates in the Philips CM30. Scanning TEM (STEM) images were recorded in the JEOL 2100F by JEOL HAADF and Gatan bright field detectors, respectively; whilst energy dispersive X-ray (EDX) analysis was obtained in the same instrument using an Oxford Instruments INCA X-Sight Si(Li) detector of 50 mm^2 area.

2.4 Atom probe tomography

Specimens for atom probe were prepared using both electropolishing and focused ion beam (FIB) liftout. Electropolished needles were prepared using a two-step process. Initially matchsticks of 0.5 mm $\times$ 0.5 mm $\times$ 20 mm were electropolished using a solution of 25 vol.% perchloric acid (60% concentration) and 75 vol.% glacial acetic acid, at a DC voltage of 14 V, until a neck formed then separated into two needle-shaped specimens [23]. The shape of these needles was further refined using a polishing solution of 2 vol.% Perchloric acid (60% concentration) in butoxyethanol. This final step was performed just prior to loading in the atom probe system to prevent oxidation of the specimens. All unaged (austenisation only) specimens were prepared using electropolishing as site specific information was not required.

For aged material, atom probe specimen were prepared by FIB method in a FEI Helios Nanolab 600 SEM following the standard lift-out procedure [24]. A protective layer of platinum was deposited on regions most likely to contain grain/lath boundaries, then a wedge of depth ~7 µm was lifted out from this protected region. Sections of the lift-out lamella were mounted onto a standard silicon microtip coupon, and each microtip was sharpened using annular milling at decreasing ion beam currents into a fine point suitable for APT analysis. The penultimate stage of this milling, carried out at 30 kV and 40 pA, removed any remaining Pt capping layer, and resulted in a specimen with a final tip radius of less than 100 nm. Finally, the sharpened tips were exposed to a 5 kV and then 2 kV ion beam for several minutes to clean the surface of any gallium ion damage [25]. At this stage, SEM side profile images of each tip were obtained to aid post-experiment 3D reconstruction of the atom probe data.

All specimens were analysed using a Cameca LEAP 3000X HR atom probe, at an analysis chamber pressure of better than $3x10^{-11}$ Torr. All samples were run in pulsed-laser mode using a

532 nm laser, operated at 0.4 nJ and 200 kHz using a base specimen temperature of 50 K. Reconstruction and analysis was performed using the commercial software IVAS version 3.6.12.

3. Results

3.1 Mechanical properties

The values of Vickers hardness HV30 (using a load of 30 kg) after different heat-treatments are given in Table 3. After ageing, the hardness values increase by approximately 70% to 90% compared to the as-austenitised conditions. Tensile stress-strain curves of the 3 heat-treatments at room temperature and 500 °C are shown in Figure 2(a). In the standard BS EN ISO 6892 the strain rate is increased at 2% strain, hence the increase in the flow stress due to strain-rate sensitivity of this material. For room-temperature tests, the ductility falls whilst the strength increases: HT3 shows a yield strength (YS) of 1892 MPa and an ultimate tensile strength (UTS) of 2009 MPa (see Table 3), which are the highest among the three heat treatment schemes. However, HT3 also exhibits the lowest tensile ductility of 2.8% (engineering strain to facture), approximately 3 times lower than the 8.1% in HT1. HT2 shows intermediate levels of YS, UTS and tensile ductility compared to HT1 and HT3. Furthermore, the YS and UTS values of all three heat treatment schemes show good correlations with the measured hardness values. As the testing temperature increases, the strength of the alloy decreases whilst the ductility improves. The changes of UTS and tensile ductility with testing temperature are given in Figure 2(b) and (c), respectively. At the highest testing temperature of 500 °C the differences of the tensile ductility among all heat-treatments diminishes to less than 1%.
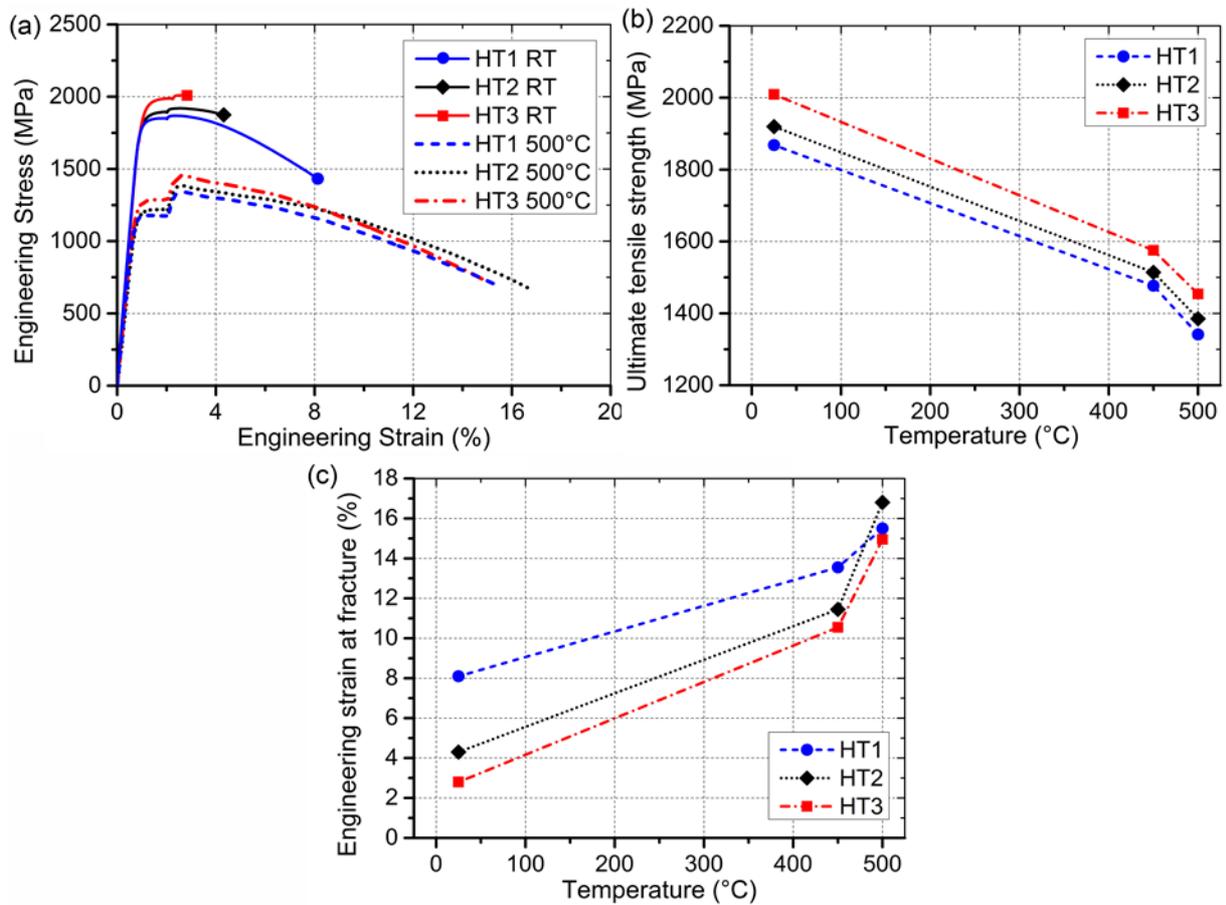
Figure 2 (a) Tensile stress-strain curves for the different heat-treatments at room temperature and 500 °C; changes of, (b) the ultimate tensile strength, and (c) the engineering strain to fracture, for the different heat-treatments at different testing temperatures.

Table 3 Mechanical testing results for samples subjected to three different heat-treatments

Sample	Hardness (HV30)		Tensile at 20 °C			Tensile at 500 °C			Creep (700 MPa at 500 °C)	
	Aust.	Aust. + Aged	Yield Strength (MPa)	UTS (MPa)	Strain to Fracture	Yield Strength (MPa)	UTS (MPa)	Strain to Fracture	Time to Rupture (h)	Minimum Creep Rate (h^{-1})
HT1	351	586	1799	1868	8.1%	1161	1341	15.5%	525	6.6×10^{-5}
HT2	341	595	1825	1920	4.3%	1181	1385	16.8%	750	2.6×10^{-5}
HT3	325	622	1892	2009	2.8%	1061	1454	15.0%	2148	6.2×10^{-6}

The fracture surfaces for HT1 and HT3 after tensile testing at room temperature and 450 °C are shown in Figure 3 and Figure 4, respectively. At room temperature, the fracture surfaces are distinctively different. For HT1, the fracture surface (Figure 3a) shows a significant amount of ductile features such as coalesced microvoids mixed with intergranular cracks. Conversely, the fracture surface of HT3 exhibits predominantly brittle fracture behaviour suggested by the

characteristic transgranular cleavage patterns (Figure 3b) [26]. These differences between fracture surfaces are consistent with the difference of tensile ductility observed between HT1 (8.1%) and HT3 (2.8%) at room temperature. At elevated temperatures the fracture surfaces of both heat-treatments exhibit more ductile features. The difference of fracture behaviours between the two heat-treatments becomes less significant. As seen in Figure 4, at 450 °C both alloys show microvoid coalescence type fracture behaviours; however, the microvoids appear to be smaller in HT1, which also displays some intergranular cracks. The tensile results are summarised in Table 3.
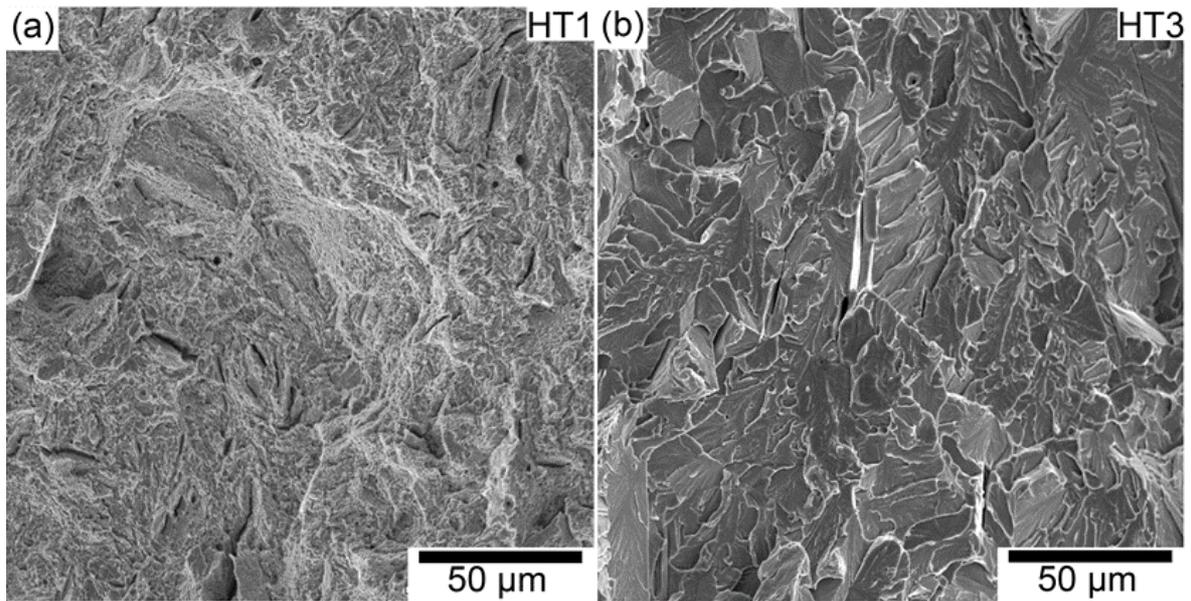
Figure 3 Fracture surfaces after tensile tests at room-temperature for (a) HT1 and (b) HT3
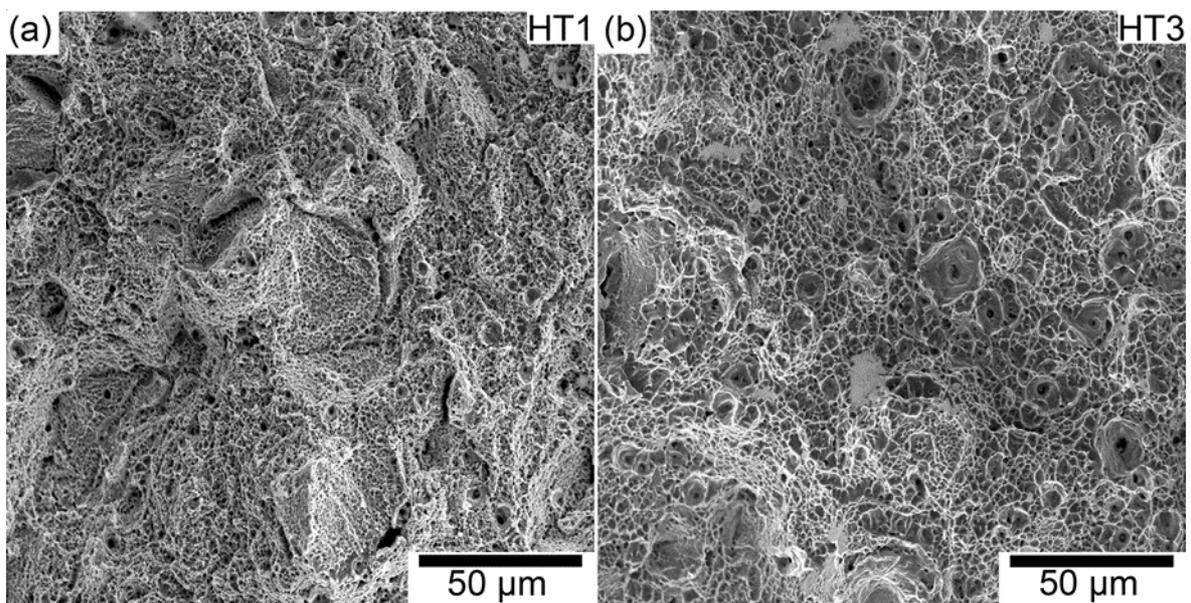
Figure 4 Fracture surfaces after tensile testing at 450 °C for (a) HT1 and (b) HT3.

9

For creep tests conducted under 700 MPa at 500 °C, the creep strain-time curves and creep rate-time plots for the three heat-treatments are shown in Figure 5(a) and (b), respectively. There are significant differences in both the minimum creep rate and the creep rupture life/ductility among the three heat-treatments: HT3 has a creep rupture life four times of that in HT1, and the creep rupture life of HT2 is between the two (see Table 3). The creep performance in terms of rupture life shows a correlation with the austenisation temperature; in this case a higher austenisation temperature gives a longer creep rupture life. The creep fracture surfaces of HT1 and HT3 (shown in Figure 6) exhibit significantly different modes of failure: HT1 appears to have failed by intergranular cracking whereas HT3 displays mainly microvoid coalescence with a smaller fraction of intergranular features.
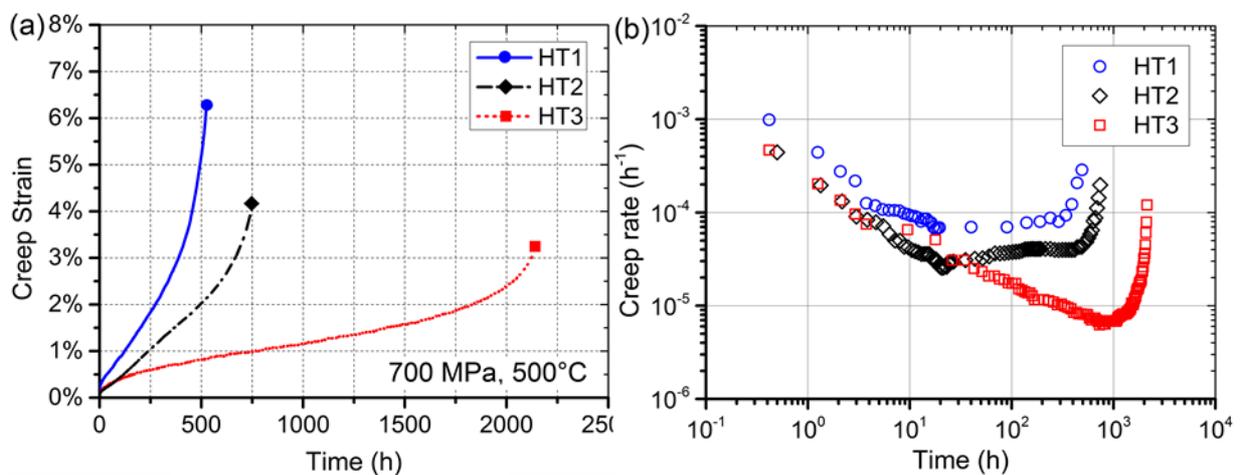
Figure 5 (a) Creep strain-time curves and (b) creep rate-time plots for the steel subjected to three different heat-treatments. The testing condition used is a load of 700 MPa at 500 °C.
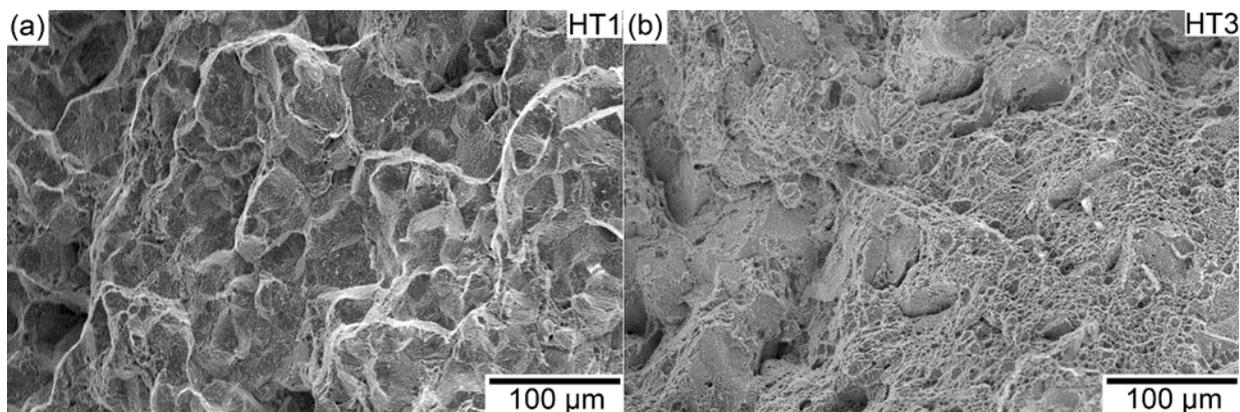
Figure 6 Fracture surfaces of creep tested (700 MPa at 500 °C) samples after (a) HT1 and (b) HT3.

3.2 Microstructures

3.2.1 The prior austenite grain (PAG) size after austenisation

The prior austenite grain boundaries (PAGBs) after austenisation were revealed after chemical etching using the solution described in Section 2.3. Optical micrographs showing typical PAG microstructures for HT1A, HT2A and HT3A are given in Figure 7(a), (b) and (c), respectively. The average PAG sizes measured by linear inception method are: 62.1±7.9 µm after HT1A, 43.7±7.0 µm after HT2A and 97.0±12.8 µm after HT3A with errors representing the standard deviations of the measurements. The highest austenisation temperature of 960 °C during HT3 gave rise to the biggest PAG size as a result of austenite grain growth. On the other hand, the longer duration of 2 hours austenisation at the lowest temperature of 825 °C during HT1 produced a PAG size bigger than that after HT2 for which the austenisation is 1 hour at 870 °C.
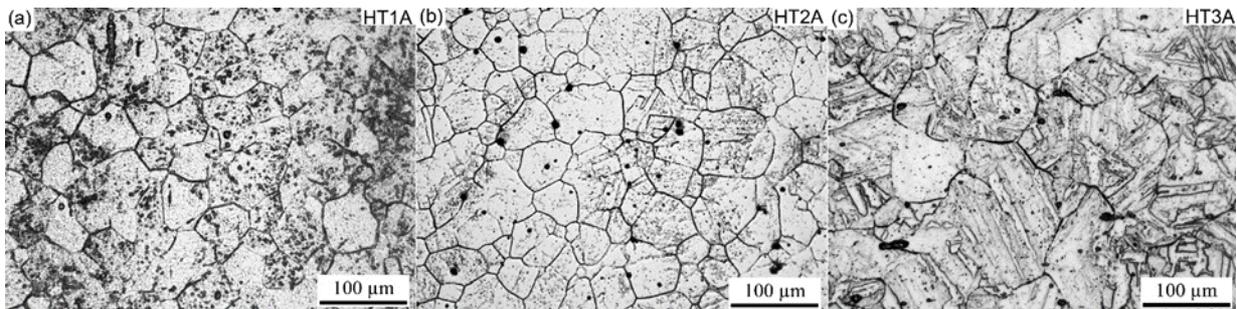
Figure 7 Optical micrographs shows the prior austenite grain structures after austenisation heat treatments in (a) HT1A, (b) HT2A and (c) HT3A.

3.2.2 The martensitic matrix

Selected areas of EBSD data representing the microstructures of the maraging steel in the as-aged conditions after the three heat-treatments are plotted as boundary maps in Figure 8. Boundaries of disorientation between 15° and 50° marked as black lines in the IPF maps and red lines in the boundary maps. As disorientations between martensitic variants are more likely to be either less than 15° or greater than 50° [27], the boundaries between 15° and 50° are most likely to be prior austenite grain boundaries (PAGBs). All samples show typical lath martensite microstructure observed in low-carbon [28] and alloyed steels [27]. The mean intercept length measured against low angle boundaries of disorientation > 2°, i.e. mainly martensite lath boundaries, for HT1, HT2 and HT3 are 1.1±0.1 µm, 1.4±0.2 µm and 1.6±0.2 µm, respectively.
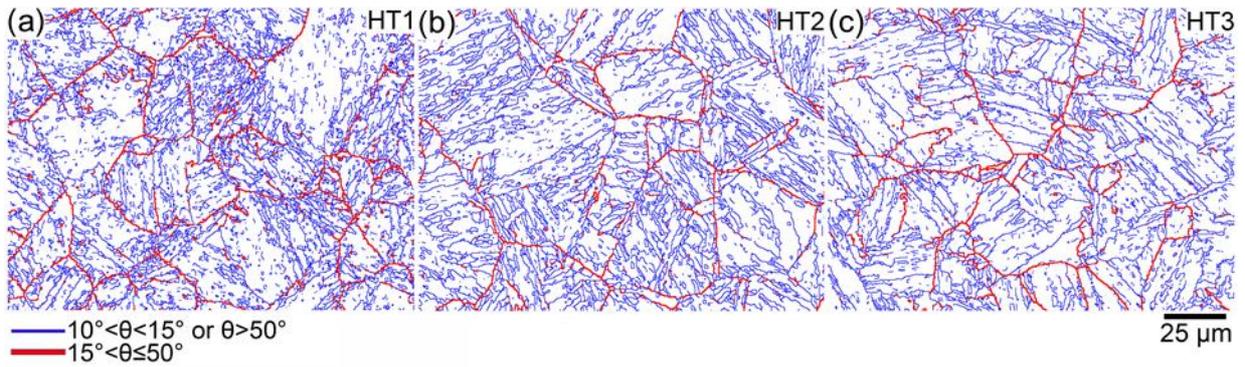
Figure 8 Microstructures of the martensitic matrix as disorientation boundaries maps in the materials subjected to (a) HT1, (b) HT2 and (c) HT3.

3.2.3 *Laves phase by STEM imaging and EDX element mapping*

Shown in Figure 9 are the micrographs by STEM-high angle annular dark field (HAADF) imaging of the microstructures after HT1 in austenitised only (HT1A) and austenitised-and-aged (HT1AA) conditions. As the bright contrast in HAADF images represents higher average atomic numbers (Z), the observed precipitates are believed to be the Mo, W and Cr-rich Laves phase predicted by the thermodynamic calculation (see Figure 1). The presence of Laves phase and its orientation relationship with the martensitic matrix is confirmed by EDX analysis and selected area diffraction (SAD) as discussed later.
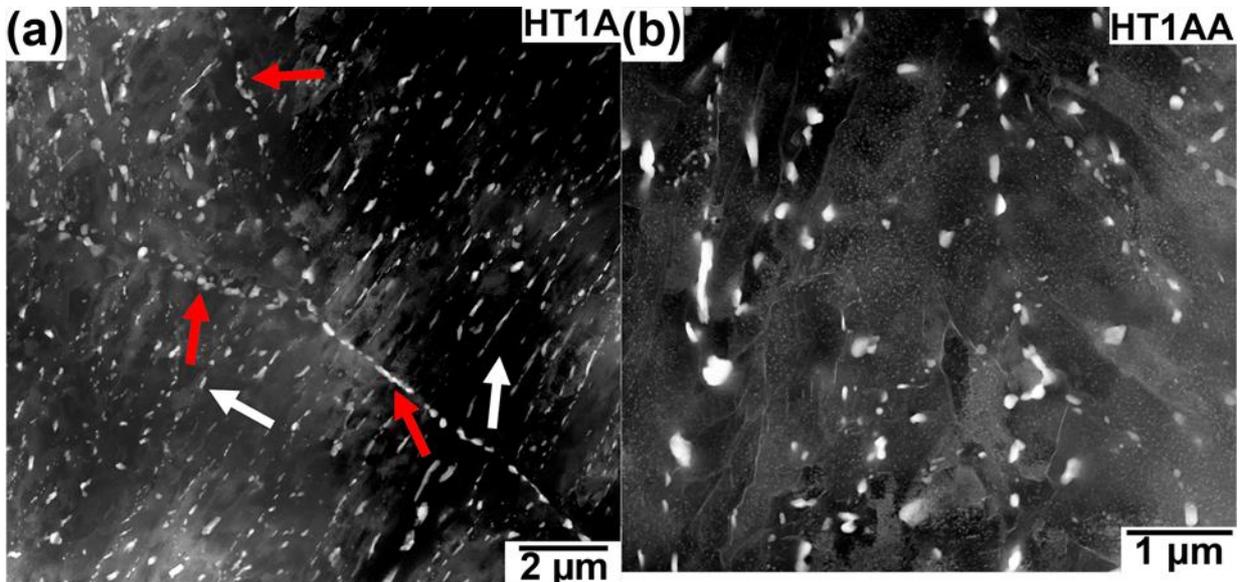
Figure 9 Typical microstructures after (a) HT1A and (b) HT1AA shown by STEM-HAADF images.

A substantial amount of large primary Laves precipitates were present in the microstructure after the low temperature austenisation at 825°C for 2 hours. These precipitates formed at PAGBs are indicated by the red arrows in Figure 9(a). They also appear to form within PAGs as pointed by the white arrows. The alignment of these precipitates suggests that they form along certain intergranular planar defects (e.g. twin boundaries) of the austenite grains. After ageing of HT1 (Figure 9b), more secondary Laves precipitates formed within the martensite laths as well as along the lath boundaries.

A qualitative EDX analysis of the primary Laves precipitates formed during austenisation after HT1A is given in Figure 10.
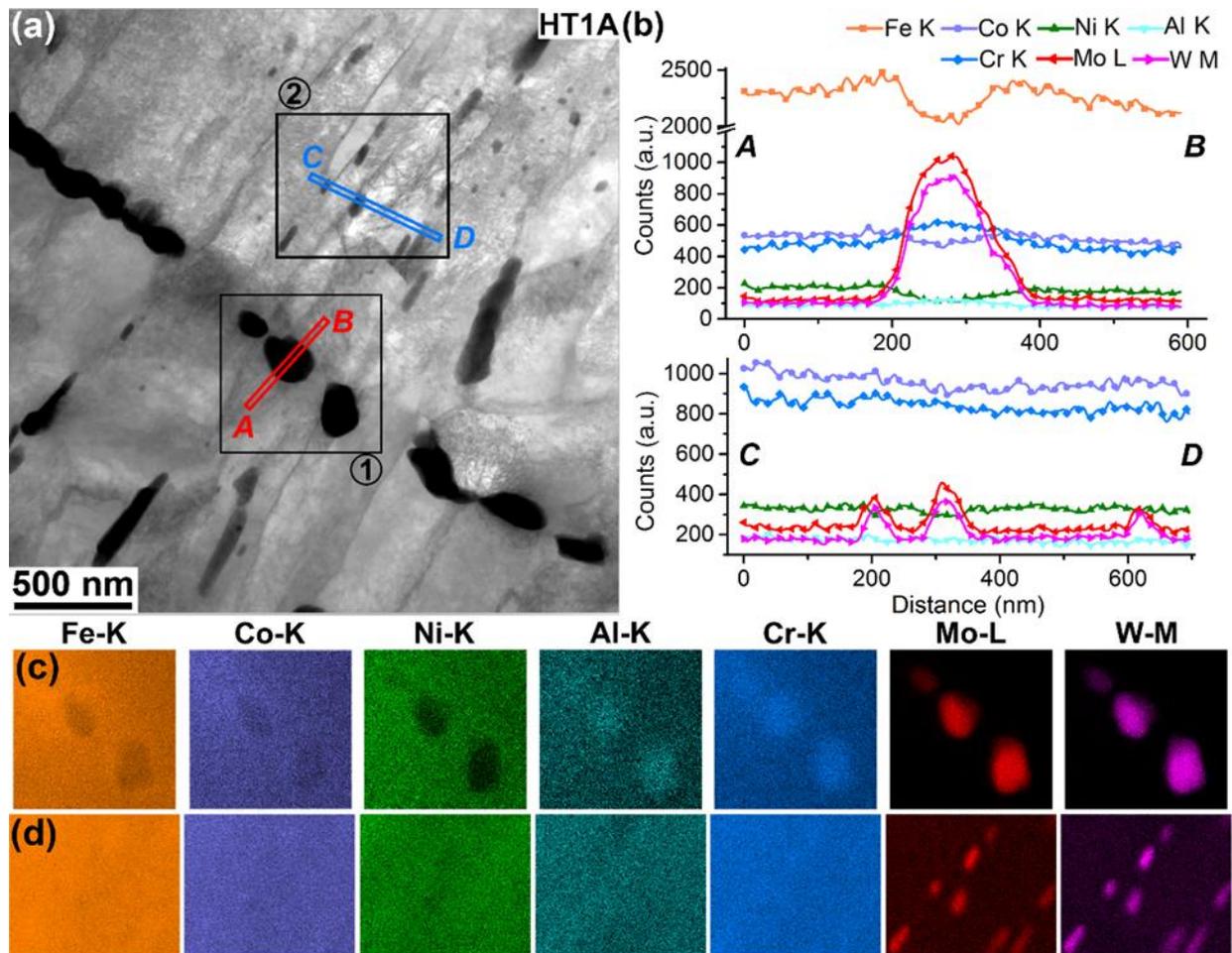
Figure 10 (a) STEM-BF images showing the primary Laves phase precipitates formed during austenisation heat treatment in HT1; (b) EDX line profiles showing the variation of the counts (arbitrary units) of major constituent elements along the scan lines AB and CD; (c) and (d) STEM-EDX elements maps showing qualitatively the distribution of major constituent elements in the rectangular selections 1 and 2 shown in the BF images, respectively,

From the element maps (Figure 10c and d), it is clear that whilst all show higher concentrations of Mo, W and Cr, the Laves phase precipitates formed on austenite grain

13

boundaries, e.g. Area 1 in Figure 10(a), exhibits greater depletions of elements such as Fe, Co and Ni compared to the ones formed within the PAGs such as those found in Area 2. This effect can be seen more clearly in Figure 10(b) by the EDX line profiles showing counts (arbitrary units) of different elements: the scan line AB shows the rejection of Fe, Co and Ni to the surrounding matrix by the formation of primary Laves phase precipitate on austenite grain boundaries; conversely, the scan line CD across several smaller intragranular primary Laves precipitates only reveals the enrichment of Mo and W when approaching the precipitates, whilst the rejection of other elements are not evident.

EDX analysis of secondary Laves precipitates after HT1AA is given in Figure 11.
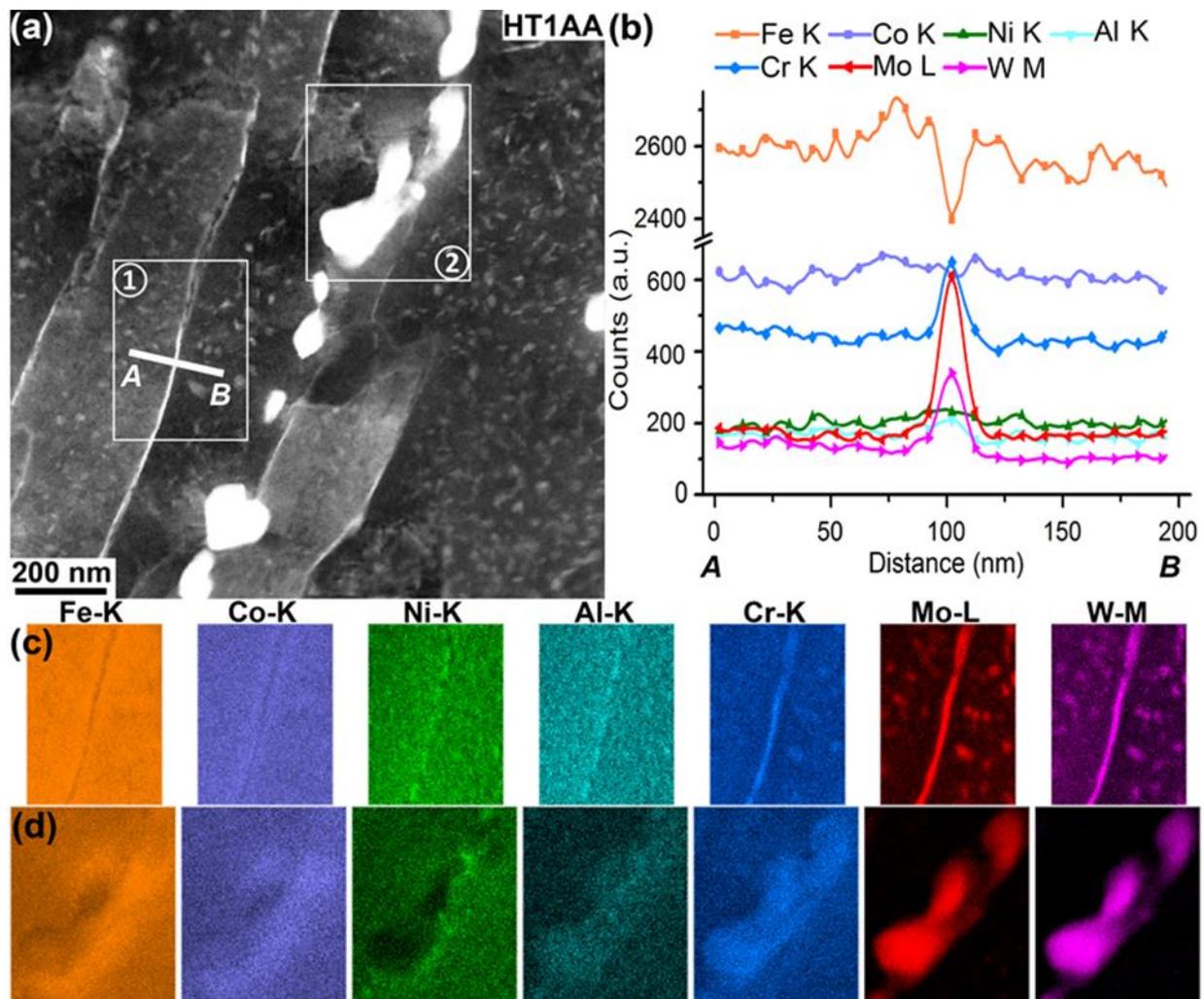
Figure 11 (a) STEM-HAADF images showing both primary Laves phase precipitates formed during austenisation and secondary Laves phase precipitates formed during ageing of HT1; (b) EDX line profiles showing the variation of the counts (arbitrary units) of major constituent elements along the scan lines AB; (c) and (d) STEM-EDX element maps of the rectangular selections 1 and 2 in the HAADF image, respectively.

Around the primary Laves phase precipitates along the PAGB (Area 2 of Figure 11a), the corresponding element maps (Figure 11d) indicate substantial enrichment of Fe, Co and Ni in the immediate vicinity of the primary Laves precipitate resulting from the rejection of these elements by its formation. In Figure 11(c), the element maps of Area 1 show the secondary Laves phase precipitates formed during ageing. Both the precipitates inside the martensite lath and along the lath boundaries were enriched with Mo, W and Cr. It also appears that Laves phase precipitates on martensite lath boundary rejected Fe and Co to the matrix adjacent to the boundary. This can be clearly seen in Figure 11(e) by the EDX line profiles along the scan line AB marked in Figure 11(a). However, in this case, the rejection of Ni is less evident. On the contrary, Ni and Al are seen in Figure 11(c) to cluster along the martensite lath boundary.

The microstructures after heat treatment for HT3A (austenitised only) are shown in Figure 12 as STEM-BF image. For HT3 after the austenisation, the lath martensite had very high dislocation densities without any noticeable precipitates.
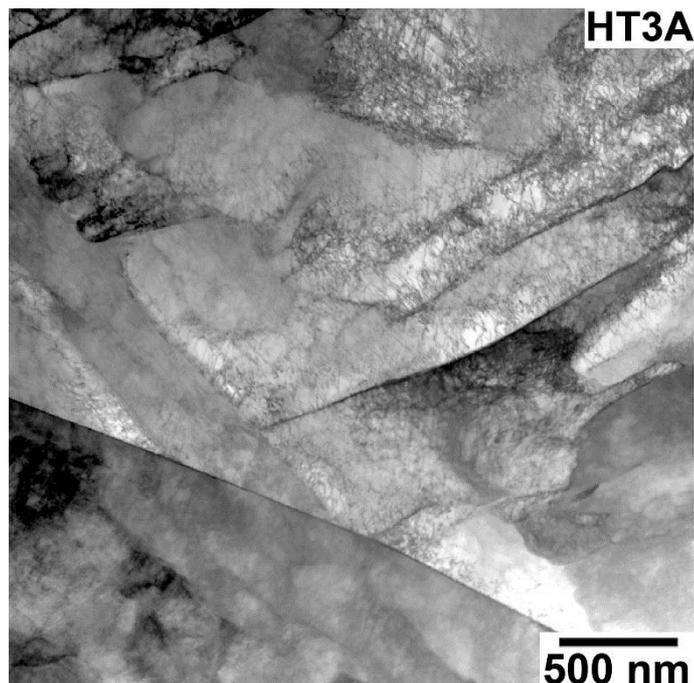
Figure 12 Typical microstructure after HT3A shown by STEM-BF image.

As shown in Figure 13(a), after the subsequent ageing heat treatment (HT3AA), a large number of precipitates were found within the martensite laths as well as along the lath boundaries. Further qualitative analysis by EDX element mapping is given in Figure 13(c). All the precipitates seen in the small selected area of Figure 13(a), both the ones inside the martensite

lath and the ones along the lath boundaries, were shown to be enriched with the constituent elements of Laves phase, i.e. Mo, W and Cr. Furthermore, the EDX line profile (shown in Figure 13d) along the scan line AB indicated higher counts of Mo, W and Cr at the lath boundaries than at the smaller precipitates within the martensite lath, probably due to the ease for diffusion and nucleation along lath boundaries.
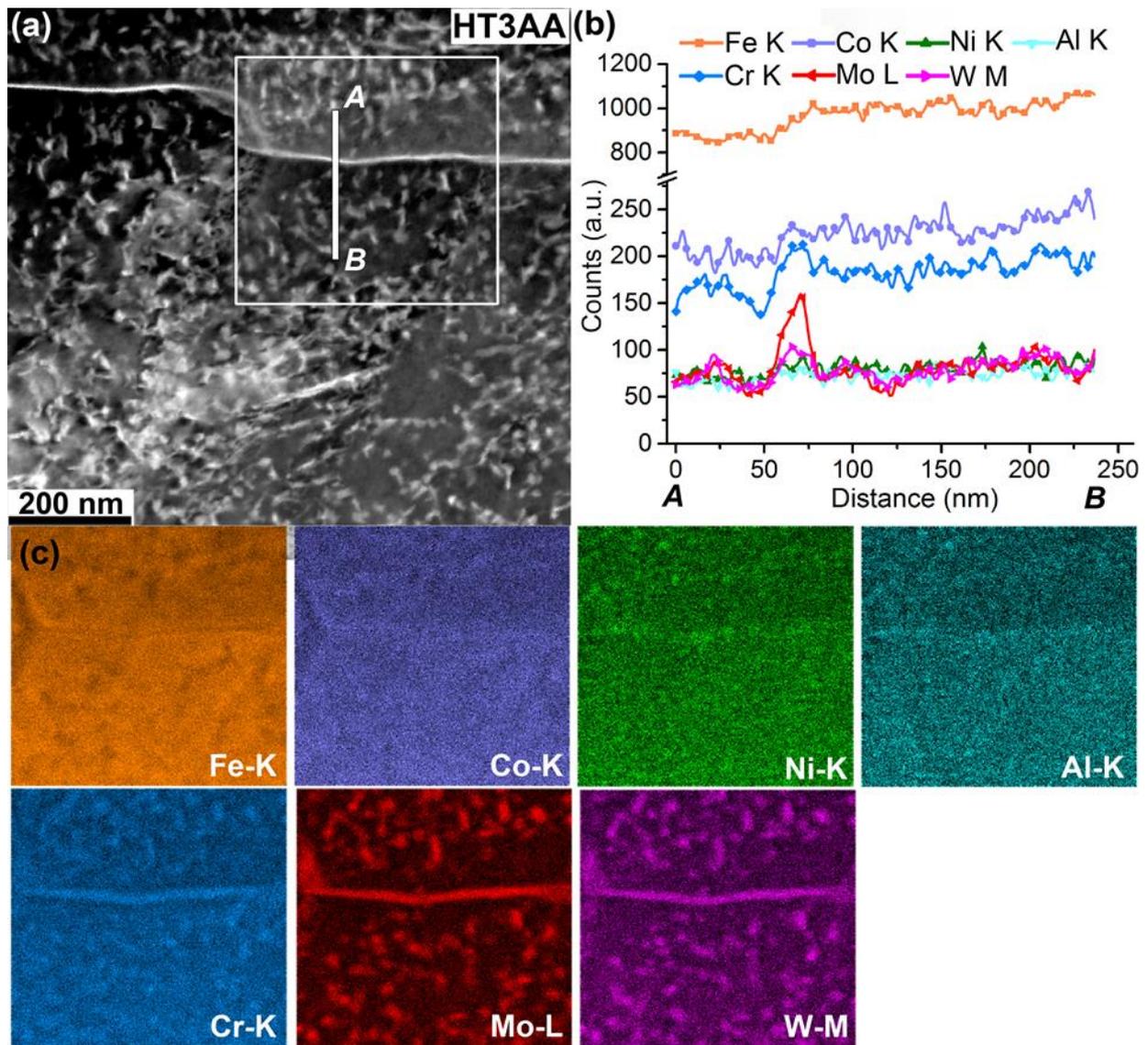
Figure 13 (a) STEM-HAADF image showing the typical microstructure after HT3AA; (b) EDX line profiles showing the variation of the counts (arbitrary units) of major constituent elements along the scan line AB; (c) STEM-EDX elements maps showing qualitatively the distribution of major constituent elements in the selected rectangular area of the HAADF image.

By manually selecting and measuring ~300 particles in high magnification STEM-HAADF images, the size distribution as equivalent circular diameter of the primary Laves precipitates after HT1A as well as of the secondary Laves precipitates after HT1AA and HT3AA are plotted as histograms in Figure 14. For HT1, the primary Laves phase precipitates formed after austenisation at 825°C for 2 hours show a broad distribution of sizes with a mean diameter of 137±8 nm; whilst after the subsequent ageing at 560°C for 5 hours, the secondary Laves phase precipitates exhibit a narrower Gaussian distribution of their sizes with a mean diameter is 18±1 nm. On the other hand, for HT3, only small secondary precipitates are present in the final microstructure, with a mean diameter of 19±1 nm and a narrower size distribution, as shown in Figure 14(c).
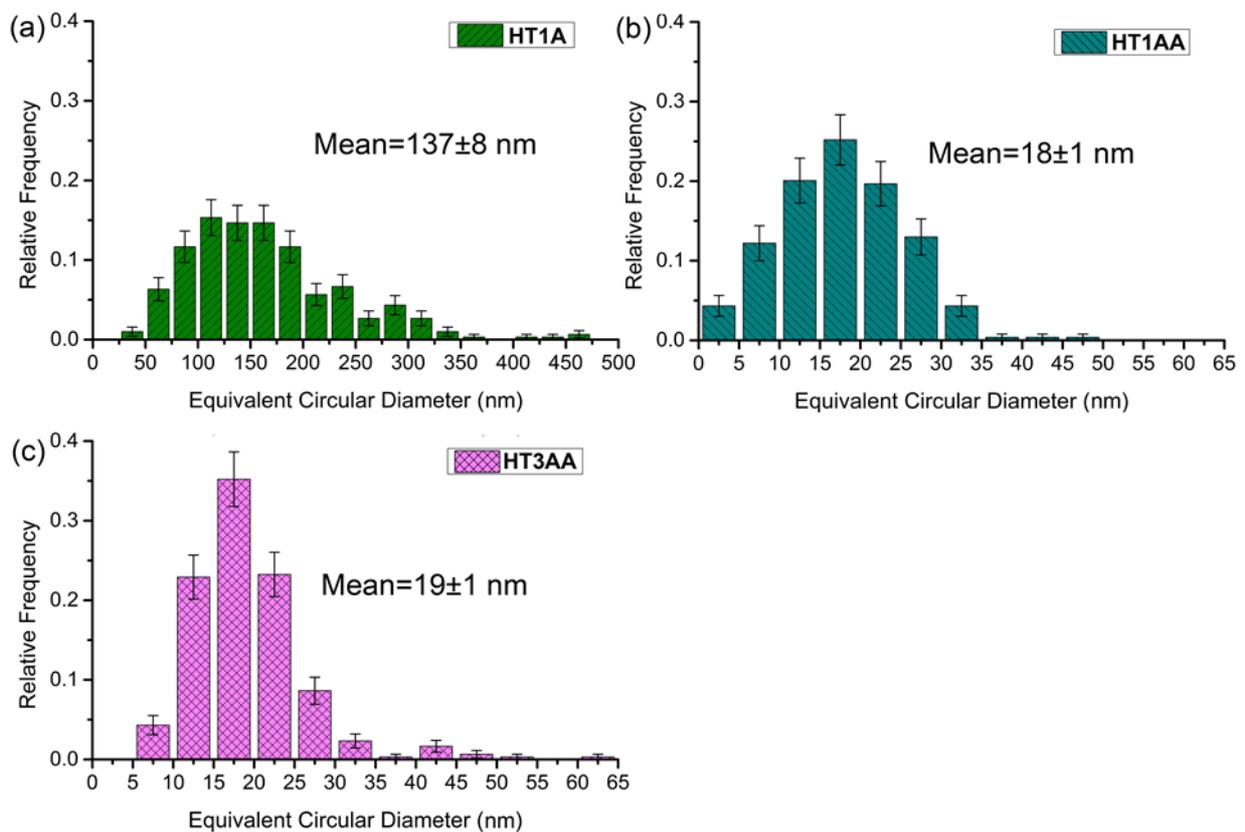
Figure 14 Histograms showing the size distributions of the Laves phase precipitates for (a) Primary Laves formed after austenisation in HT1, (b) secondary Laves formed after ageing in HT1 and (c) the secondary Laves formed after ageing in HT3.

In summary, in HT1 there are two types of W- and Mo-rich Laves phase precipitates present, with distinctively different sizes. After austenisation, large primary Laves are formed, whilst small secondary Laves are formed during the ageing process. For the same steel subjected to HT3, no Laves precipitate is observed after austenisation, and only after ageing do the small secondary

17

Laves phase precipitates form in the microstructure, located both within the martensite laths and along the lath boundaries.

3.2.4 *β-NiAl by TEM selected area diffraction and dark field imaging*

As predicted by the thermodynamics calculation (see Figure 1), in addition to the Laves phase precipitates, a comparable amount of β-NiAl precipitates should be present in the alloy at ageing temperatures used in this study under equilibrium conditions. However, direct characterisation of these β-NiAl precipitates using TEM remains challenging due to their very small size (usually <10 nm in diameter), little diffraction contrast as a result of full coherency with the ferrite matrix with a lattice misfit strain <1% [18] (the bulk lattice parameter is ~0.2887 nm for β-NiAl and ~0.2866 nm for the ferrite [17]). Furthermore, the average atomic number of β-NiAl precipitates is similar to the matrix, giving low atomic number (Z) contrast under STEM-HAADF mode. Fortunately, the ordered structure of β-NiAl precipitates gives rise to superlattice reflections in selected area diffraction patterns (SADP), which are the forbidden reflections of the disordered ferrite matrix. Therefore, TEM-dark field (TEM-DF) technique using the superlattice reflection can be exploited to image β-NiAl precipitates in this alloy after the ageing.

One such example of the alloy after HT1AA is given in Figure 15. The BF micrograph (Figure 15a) reveals several large secondary Laves precipitates by diffraction contrast. The insertion shows the SADP of this area taken with incident electron beam parallel to the [101] ferrite/ β-NiAl zone axis. The weak $\{111\}_\beta$ and $\{110\}_\beta$ superlattice reflections can be readily identified as well as the DPs from Laves phase precipitates. It also appears that the $[11\bar{2}0]_L$ zone axis of the Laves phase is parallel to the [101] ferrite zone axis. The same type of orientation relationship was reported recently between C14 structured $(FeCrSi)_2(MoNb)$ Laves phase and the type 444 ferrite stainless steel matrix [29]. The DF micrograph taken from $(0\bar{1}0)_\beta$ superlattice reflection (labelled as A in the SADP) of the same area is given in Figure 15(b), showing a large amount of fine β-NiAl precipitates that are not visible in the BF micrograph.

Similarly, BF image SADP analysis of the alloy subjected to HT3AA are shown in Figure 15 (c) and lower insertion, respectively. The DF image (Figure 15d) was taken with the incident electron beam parallel to the $[01\bar{1}]$ ferrite zone axis. In this case, the β-NiAl precipitates appear to be smaller than those found after HT1AA, probably due the lower ageing temperature of 540 °C used in HT3. SADP+DF did reveal the presence of β-NiAl precipitates in this alloy after ageing heat treatment, however, more quantitative information such as size distribution will be better studied by APT presented in the next section.
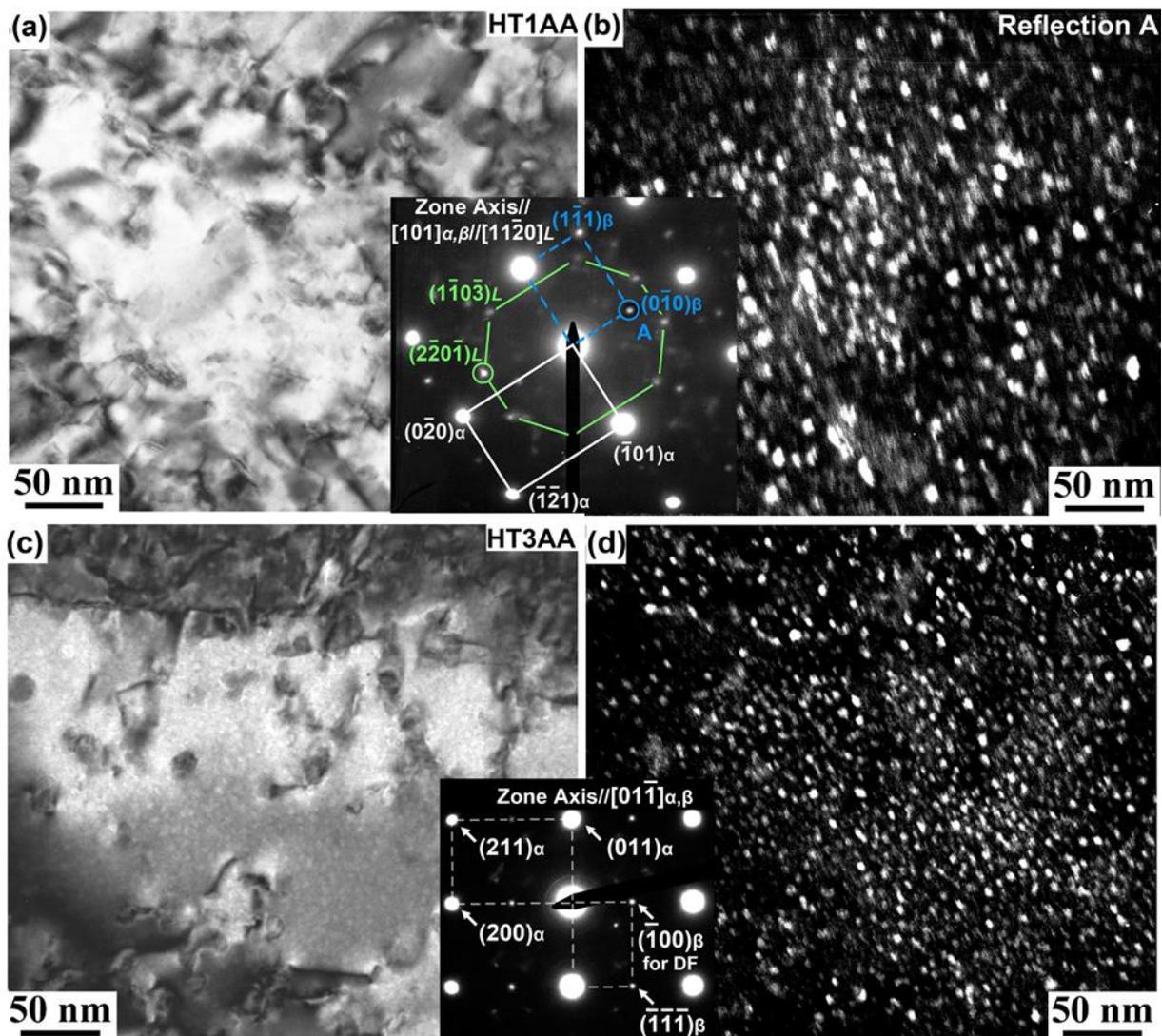
Figure 15 (a) TEM BF micrograph after HT1AA with SADP in insertion showing ferrite, β-NiAl superlattice and Laves phase reflections; (b) DF image of the same area of (a) using the β-NiAl $(0\bar{1}0)_\beta$ superlattice reflection labelled as A in the SADP. (c) BF micrograph after HT3AA with SADP in insertion, (d) DF image of the same area of (c) using the β-NiAl $(\bar{1}00)_\beta$ superlattice reflection.

3.2.5 *Atom probe tomography*

Typical atom maps showing elements distribution in 5 nm thin slices of the reconstructed 3D APT datasets in materials after HT1AA and HT3AA are given in Figure 16, with the Laves phase indicated by clusters of red Mo atoms and the β-NiAl precipitates by green Ni and light blue Al atoms. APT results show a marked difference in the size and spacing of β-NiAl precipitates between the two heat treatments. In the HT1AA samples (Figure 16a), the β-NiAl particles are larger and more varied in shape, whilst in the HT3AA specimens (Figure 16b) these particles are

19

smaller and largely ellipsoid. Furthermore, after the HT3AA heat treatment, the β-NiAl particles also show a more uniform number density across all datasets studied, in contrast to the wider variations seen in the HT1AA specimens.
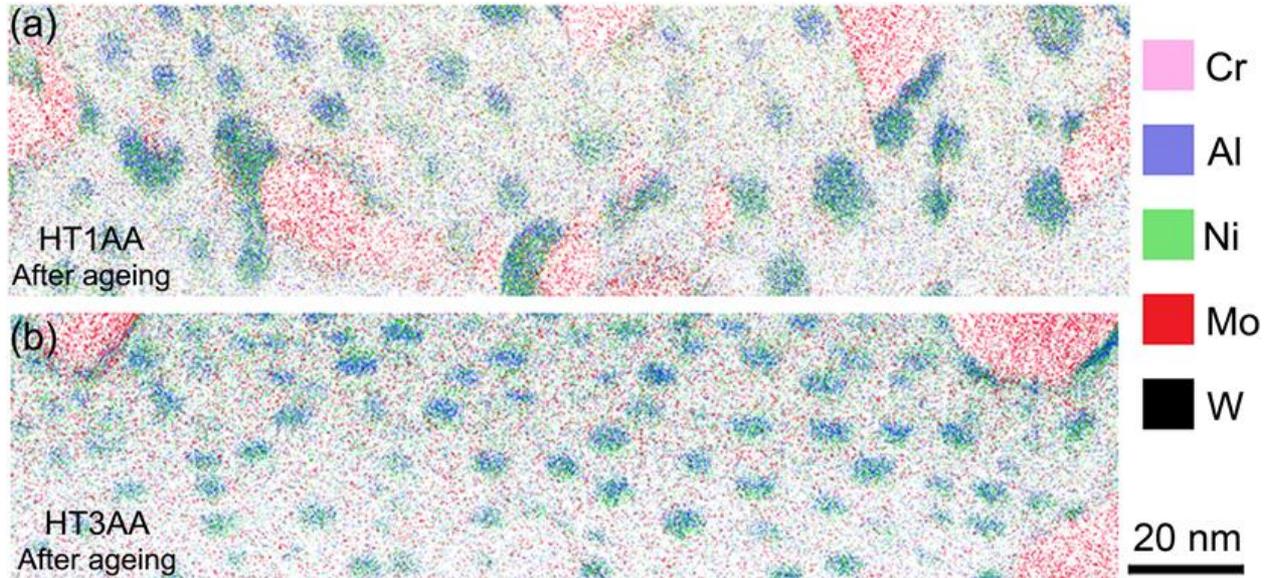
Figure 16 Atom maps of typical samples (a) after HT1AA and (b) after HT3AA. For clarity and ease of comparison only Ni (green dots), Al (blue dots) and Mo (red dots) atoms are shown and volumes are restricted to 5 nm thick slices.

Isoconcentration surface is commonly used in APT to differentiate precipitates and phase boundaries, and variations caused by the choice of isoconcentration threshold values are small [30]. Isoconcentration surfaces of 6 at.% Mo and 15 at.% Ni were found to most effectively discriminate the Laves phase and β-NiAl precipitates respectively from the matrix. The details of all isoconcentration surfaces across each dataset were exported for statistically morphological analysis. Only complete particles (i.e. precipitates wholly contained in the APT reconstruction, not intersecting with the surface) were included for calculation. The measurements were averaged across all datasets for each heat treatment condition and normalised by the dataset size. The size distribution of β-NiAl precipitates as histograms of equivalent circular diameters (ECDs) is shown in Figure 17. A summary of these results is given in Table 4.
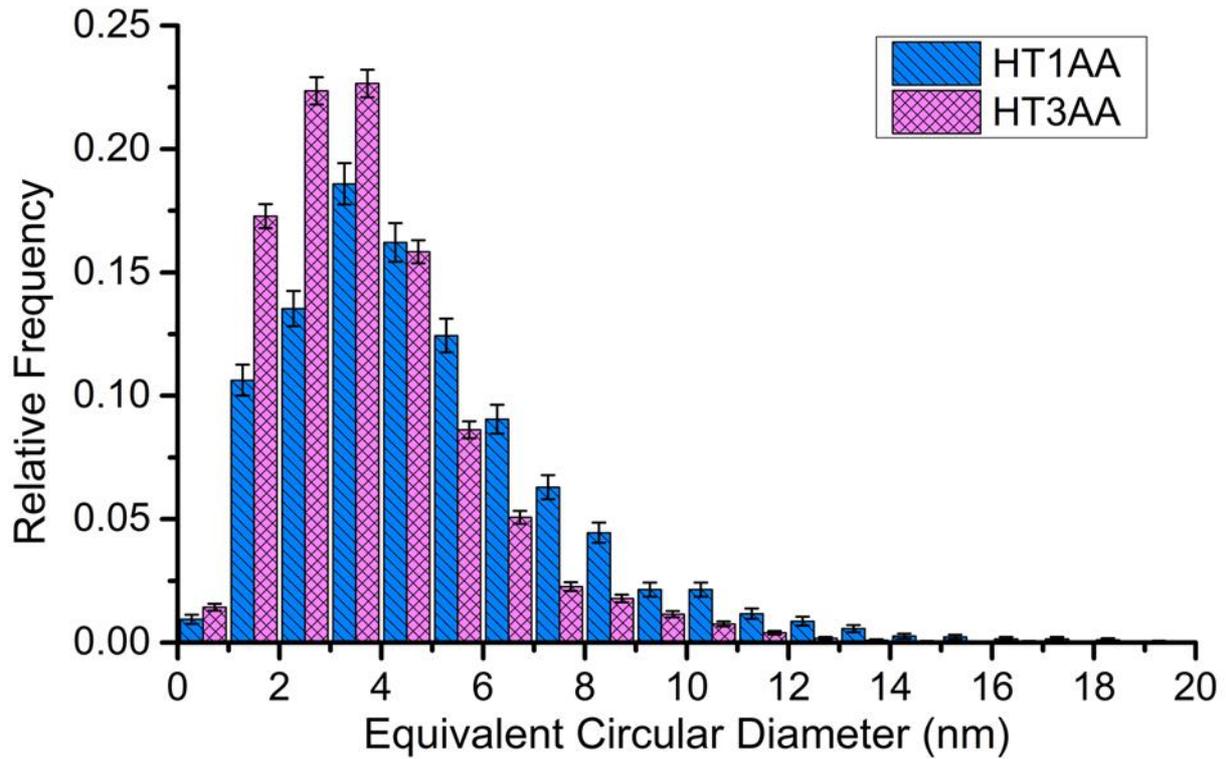
Figure 17 Histograms showing the size distributions of the β-NiAl phase precipitates after heat treatment HT1AA and HT3AA.

Table 4 Statistical analysis of the distribution of the secondary Laves phase precipitates and β-NiAl precipitates in the maraging steel after heat treatment HT1AA and HT3AA.

Heat treatment	HT1 A+A			HT3 A+A	
Phase	β-NiAl	Primary Laves phase	Secondary Laves phase	β-NiAl	Secondary Laves phase
Average Equivalent Circular Diameter, d_{ECD} (nm)	5.2±1.0	137±8.3 [*]	17.8 ±1.0 [*]	3.8±0.3	19.1±0.8 [*]
Number of precipitates per 1 million ions	20.0±3.0	N/A	N/A	63.6±40.1	N/A
Number density, N_v (m^{-3})	16.7×10^{23}	0.012×10^{23} [#]	0.22×10^{23} [#]	53.2×10^{23}	0.19×10^{23} [#]
Volume Percent, V_f	12.1 % [+]	1.6 % [‡]	6.4 % [‡]	15.7 % [+]	6.8 % [‡]
Inter-particle spacing (nm) [31]	25	5.6×10^3	174	14	175

[*] measured by TEM; [‡] determined by the "lever rule" method using APT data according to Ref. [18, 32]; [#] calculated based on V_f from APT data using the lever rule method and d_{ECD} measured by TEM; [+] calculated from number density (N_v) and d_{ECD} measured by APT according to Ref. [19].

To derive the spatial distribution characteristics of the precipitation phases listed in Table 4, a number of methods were used. For the smaller and almost spherical β-NiAl precipitates, the

number density can be readily measured by APT, and the volume fraction can be estimated by [19]:

$$V_\beta = \frac{4}{3}\pi r_\beta{}^3 N_v \qquad (1)$$

where V_β is the volume fraction of β-NiAl, r_β is the mean radius and N_v is the number density of β-NiAl precipitates measured by APT.

For the larger and complex shaped Laves phase particles (both primary and secondary), measuring the number density by APT is difficult whilst approximating their shape as sphere is inaccurate. Therefore, the above method described in Eq.(1) is not suitable for Laves phase. Conversely, the composition of the Laves phase can be determined reliably by APT. Therefore, the Lever rule method [18, 32] is better suited to derive the volume fraction of Laves phases:

$$V_L \approx \frac{C_o - C_\alpha}{C_L - C_\alpha} \qquad (2)$$

where V_L the volume fraction of Laves phase particles, C_o, C_α and C_L are the concentrations of the partitioning alloying elements in the bulk, the martensitic matrix and the Laves phase precipitate, respectively. Average value of V_L were calculated using only concentrations of Mo and W as these two elements predominately partitioned between Laves phase and the martensitic matrix with very little in solid solution of the β-NiAl (see Table 5 to Table 7).

Finally, the inter-particle spacing λ can be expressed as:

$$\lambda = \frac{4(1 - V_f)r}{3V_f} \qquad (3)$$

where V_f is the volume fraction of the precipitates and r is the corresponding mean radius [31].

From Table 4, the β-NiAl precipitates on average are larger and spaced further apart after HT1AA than after HT3AA, whilst the number density is ~3 times higher in the latter. The size distribution histogram shows clearly that the number of larger β-NiAl precipitates (ECD > 5nm) is substantially higher after HT1AA compared to narrower distribution in HT3AA. This difference is believed to be the result of different ageing temperature (560 °C in HT1 and 540 °C in HT3), i.e. higher ageing temperatures led to coarser and less frequent β-NiAl precipitates with a wider size distribution.

The isoconcentration surfaces were also used to separate the atoms belonging to each phase into separate datasets for comparison of the precipitate chemistry. Regions with >6 at.% Mo and

>35 at.% Ni were used to extract only the atoms within the centre of the Laves phase and β-NiAl particles, respectively. To obtain the matrix composition, regions with <2.5 at.% Mo and <15 at.% Ni were isolated. By extracting each into isolated datasets phase without the overlapping interfacial regions, each could then be separately analysed. This is important as a significant peak overlap exists in the mass spectrum for this material at 27 Da, which can correspond to the +1 charge state of ^{27}Al as well as the +2 charge state of the ^{54}Fe isotope, as discussed further in [33]. Due to the very segregated nature of Al in this maraging steel after ageing, in the β-NiAl precipitates the 27 Da peak was made up almost entirely by ^{27}Al^{1+}, whilst within the matrix this peak was dominated by ^{54}Fe^{2+}. Although this peak overlap can be deconvoluted by IVAS based on the other isotopes present, this can only be done globally, and the fact that Al has only a single isotope makes the deconvolution challenging. By extracting the β-NiAl particles and matrix to separate datasets, the deconvolution can be applied to each region separately, which obtains far more reliable chemical compositions of the different constituent phases in this alloy.

Table 5 gives the chemical composition for the matrix after various heat treatment conditions. The compositions of the matrix after HT1A and HT3A are very similar to the initial bulk composition given in Table 1. After ageing, due to the precipitation of the intermetallic phases, the martensite matrix sees substantial depletion of Ni, Al, Mo and W whilst Co and Cr concentrations show little change.

Table 5 Matrix composition after various heat treatments obtained by APT (in at.%); error represents the weighted standard deviation among multiple APT samples.

Heat Treatment	Fe	Cr	Co	Ni	Al	Mo	W
HT1A (Aust. Only)	68.8±0.5	10.8±0.1	7.7±0.2	6.5±0.5	3.6±0.1	1.5±0.2	0.6±0.1
HT3A (Aust. Only)	69.5±0.5	10.8±0.1	7.6±0.1	6.0±0.2	4.0±0.7	1.6±0.1	0.6±0.2
HT1AA (Aust.+Aged)	77.2±1.5	10.7±0.8	7.2±0.8	2.5±0.7	1.6±1.0	0.6±0.2	0.1±0.1
HT3AA (Aust.+Aged)	77.3±2.9	10.6±1.4	7.5±0.4	2.5±0.8	1.1±0.1	0.8±0.3	0.2±0.1

Table 6 summarises the composition of the primary Laves phase in the unaged HT1 sample and the secondary ones in aged HT1 and HT3 materials. The W content of the primary Laves phase precipitate formed during austenisation at 825 °C is significantly higher than that of the secondary precipitates formed during ageing at 540 / 560 °C. Furthermore, the Cr and Ni contents

of the primary Laves phase precipitate are substantially lower than those of the secondary ones. All these observations are in good agreement with the predicted composition of Laves phase as a function of temperature shown in Figure 1(b). The only contradiction is the Mo content, where prediction suggests higher values in the secondary Laves phase formed at lower temperatures; however, the measured Mo content is higher in the primary one. This could be due to limited sampling by the APT method as the size of the primary Laves phase precipitate (with an ECD of 137 nm) could be bigger than an APT sample. For the secondary Laves phase precipitates formed after HT1AA and HT3AA, the compositions are very similar to each other, and also consistent with the predictions made by MatCalc with MC_Fe_2.009 database shown in Figure 1(b).

Table 6 Compositions of the Laves phase precipitates (in at.%); error represents the weighted standard deviation among multiple APT samples.

Heat Treatment	Fe	Cr	Co	Ni	Al	Mo	W	Si
HT1A Aust. Only (Primary) [*]	44.9	10.9	5.1	1.4	0.6	21.0	14.8	1.0
HT1AA Aust.+Aged (Secondary)	43.8±2.3	21.1±0.9	5.6±0.7	4.1±1.8	0.6±0.4	16.6±0.6	6.5±2.3	1.4±0.4
HT3AA Aust.+Aged (Secondary)	42.1±6.2	22.3±3.0	6.0±0.5	3.5±0.8	0.4±0.2	17.1±6.1	6.4±4.0	1.1±0.1

[*] For material subjected to HT1A, only one out three APT samples contained part of a primary Laves phase precipitate, therefore the measurement uncertainty cannot be estimated.

Similarly, the compositions of β-NiAl precipitate formed during ageing (presented in Table 7) are broadly similar between the two heat treatments, with roughly equal atomic concentrations of Ni and Fe as well as slightly higher percentages of Al. However, some discrepancies are observed between the measured composition of β-NiAl and the predicted ones shown in Figure 1(c), as the MatCalc calculation indicates a β-NiAl composition of ~50 at.% Ni, 30 at.% Al and 20 at.% Fe between 540 °C and 560 °C. Further discussions on the compositions of precipitates are presented in Section 4.1.

Table 7 Comparison of the β-NiAl particle composition after the two ageing treatments obtained by APT (in at.%); error represents the weighted standard deviation among multiple APT samples.

Heat Treatment	Fe	Cr	Co	Ni	Al	Mo	W
HT1AA (Aust.+Aged)	25.1±3.9	3.4±0.2	4.5±0.3	30.0±6.0	36.3±7.1	0.3±0.2	0.1±0.1
HT3AA	28.0±1.9	4.3±0.7	4.1±0.5	26.3±8.1	36.0±7.9	0.5±0.12	0.2±0.1

The key observations from the compositional information in Table 5 to Table 7 and the morphological analysis in Table 4 show that whilst the chemical compositions of the precipitation phases as well as the martensitic matrix are insensitive to the 20 °C difference of the ageing temperatures between HT1 and HT3, the APT analysis clearly indicates significant differences in the size and spatial distribution of the β-NiAl particles as a result of the 20 °C difference. The β-NiAl are larger and spaced further apart in the HT1AA sample, and less numerous; whilst the β-NiAl particles after HT3AA are smaller and much more numerous.

4. Discussion

4.1 The composition and distribution of precipitation phases

For the secondary Laves phase precipitates formed during ageing, the measured compositions (see Table 6) can be roughly expressed as 43Fe-22Cr-6Co-4Ni-17Mo-6.5W-1Si-0.5Al (at.%), which is in reasonable agreement with the equilibrium composition predicted by MatCalc. The measured ratio of atomic concentrations between Fe+Cr and Mo+W is 2.77, whilst the predicted value is ~2.6. Albeit both are higher than the stoichiometric value of 2, these values are well within the reported range between 2.36 to 2.88 for Laves phase precipitates formed during creep testing at 650 °C in a Co (3 wt.%) modified P911-type steel [34]. Among the major constituent elements, the differences between the measured and predicted concentrations of Mo and W are less than 0.5 at.% and 2 at.%, respectively; whilst the measured Fe content is ~9 at.% higher and the measured Cr content is ~6.5 at.% lower than predicted equilibrium values. For minor constituent elements of the Laves phase, the measured Ni content is ~4 at.% which is about half of the predicted level of 8 at.%; furthermore, around 6 at.% of Co was found in the secondary Laves phase precipitates which was not predicted by the thermodynamics calculation using the MC_Fe_2.009 database.

The observed differences between measured and predicted compositions could simply be due to equilibrium state not being reached for the Laves phase precipitate after ageing for 5 hours. A TCP R-phase is believed to be metastable and precede the precipitation of the C14 Laves phase [35]. Work on a Fe-10Cr-1.4W-4.5Co (at.%) steel showed the presence of R-phase after ageing at 600 °C for 1000 hours [36]. A detailed study [37] of the R-phase composition in maraging steels of the Fe-Cr-Ni-Co-Mo system showed that although the concentrations of elements in R-phase precipitates vary with base steel composition and ageing conditions, the overall atomic ratio is

centred around 40Fe-20Cr-7Co-3Ni-30Mo (at.%), which is quite similar to the composition of the secondary Laves phase precipitates measured in the present study. Therefore, it is possible that after ageing for 5 hours, some metastable R-phase precipitate could be present in this maraging steel among the Laves phase, which contributed to the deviations from the equilibrium compositions.

In addition, more than 1 at.% of Si was found in the secondary Laves phase precipitates in the current work. Interestingly, various previous studies [21, 38-40] have showed the important role played by Si in accelerating the precipitation kinetics of Laves phase particles in 9-12% Cr steels. Significant concentrations of Si were reported in the Laves phase precipitates found in these studies. For example, Aghajani *et al.* [39] reported an average of 7 at.% of Si in Laves phase particles in a 12% Cr martensitic steel containing only 0.15 wt.% of Si in bulk. As Si is an impurity in the maraging steel studied in this work with bulk concentration < 0.05 wt.%, the presence of >1 at.% Si in the vast majority of these precipitates reaffirms the predominant presence of Laves phase. Furthermore, Hosoi *et al.* [40] showed that decreasing Si content from 0.29 to 0.008 wt.% increases the time required to form Laves phase by a factor of almost 100 at 600 °C (values taken from Fig. 9 of Ref. [40]) for 9Cr-2Mo steels. Similarly, the very low Si content in the current steel probably contributed to the slow precipitation kinetics of secondary Laves phase precipitates leading to the observed deviations from predicted equilibrium compositions.

For β-NiAl, precipitates which were formed solely after ageing heat treatment at 540 °C and 560 °C, the following points are observed for the measured composition (see Table 7): (i) Al is ~5 at.% higher, (ii) Ni is 18-22 at.% lower, (iii) Fe is 4-8 at.% higher than the predicted equilibrium values and (iv) the presence of Cr, Mo W and Co which were not predicted by MatCalc with MC_Fe_2.009. One possible explanation for the observed discrepancies is that similar to secondary Laves phase, after ageing for 5 hours the equilibrium composition of β-NiAl had not been reached. Studies on β-NiAl in C-free PH13-8Mo steel [14], low carbon Alloy1014 steel [41] and a medium carbon secondary hardening steel [42] all found that with increasing ageing time, the concentrations of Ni and Al increased whilst the Fe content decreased. Therefore, it is possible for the current steel with increasing ageing time, the Ni and Fe content could converge towards predicted equilibrium values. Admittedly, this will probably lead to even higher Al concentration in β-NiAl than predictions. Furthermore, Cr, Mo and/or Co were also found to be soluble in the β-NiAl precipitates in different steel systems [14, 32, 42]. These observations all suggest that the precipitation chemistry of β-NiAl is more complex than simple

thermodynamics based calculation predicts. The actual alloy compositions, especially the variation of the martensitic matrix composition prior to the ageing heat treatment due to the precipitation of primary Laves phase during austenisation in HT1, could affect the precipitation behaviour of β-NiAl as well. Nevertheless, comparing the β-NiAl precipitates formed after HT1 and HT3, the differences are small.

Conversely, the different ageing temperatures had significant effects on the spatial distribution characteristics of the β-NiAl precipitates as shown in Table 4. The measured mean is ~30% smaller after ageing at the lower temperature of 540 °C in HT3AA, whilst the estimated volume fraction is ~30% higher. The effects on precipitation number density and inter-particle spacing are even more profound, with the number density being >200% higher and the inter-particle spacing being ~45% lower after HT3AA when compared to those values after HT1AA. For HT1AA, the estimated volume fraction (12.1 vol.%) of β-NiAl by APT is in good agreement with that predicted by MatCalc (10.9 vol.%), as shown in Figure 1(d). For HT3AA, the difference between the 15.7 vol.% from APT and predicted 10.8 vol.% by MatCalc is noticeably bigger.

The volume fraction derived by the lever rule method for the primary Laves phase after HT1A is 1.6 vol.%, which is lower than the 2.5 vol.% predicted by MatCalc. For the smaller secondary Laves phase precipitates, the volume fractions derived by APT (6.4 vol.% after HT1AA and 6.8 vol.% after HT3AA) are also slightly lower than the predicted values by MatCalc (8.6% and 8.5%, respectively). Interestingly, the mean size and volume fraction of the secondary Laves phase precipitates after HT1AA are both slightly lower than those after HT3AA despite the fact that the ageing temperature (560 °C) of HT1AA is 20 °C higher than that of HT3AA (540 °C).

In summary, whilst the 20 °C difference of ageing temperatures did not show strong impact on the chemical compositions of the β-NiAl precipitates, it did exert strong influence on the spatial distribution characteristics of the β-NiAl particles. For the Laves phase, the 20 °C difference had negligible effect on both the chemical composition and spatial distribution of the secondary Laves phase precipitates. The subsequent influences on mechanical properties are discussed in the next section.

4.2 Effect of heat treatment on mechanical properties

The basic factors contributing to the room temperature yield strength for martensitic steels are solid solution strengthening, dislocation strengthening, sub-boundary strengthening, and precipitation strengthening [43]. As the extent of solid solution strengthening, dislocation

strengthening and sub-boundary strengthening are not expected to differ significantly in materials after HT1AA and HT3AA, the focus of the discussion is placed on the factor that could be affected by the different heat treatments, i.e. the precipitation strengthening mechanism.

For coherent precipitates, depending on the size, the contribution to the increases of yield strength is achieved through either the Orowan dislocation bypassing (looping) or particle cutting (shearing) mechanisms [44]. The critical radius r_{crit} of the precipitate above which the strengthening mechanism switches from particle shearing to Orowan looping is generally believed to be only a few nanometres [45]. For the β-NiAl precipitates in PH13-8Mo steel, r_{crit}=3.8 nm (or d_{crit}=7.6 nm) is obtained through the best reproduction of experimental yield strength trend by thermo-kinetic simulation [46]. Most of the β-NiAl precipitates after both HT1 and HT3 in this steel are smaller than the critical size of d_{crit}=7.6 nm (see Figure 17). Therefore, the contribution from β-NiAl precipitates to yield strength is predominately by particle shearing mechanism. Conversely, for the incoherent secondary Laves phase precipitates, the size distributions shown in Figure 14 indicate that the majority of the particles have diameters greater 10 nm with mean d_{ceq} approaching 20 nm. Therefore, Orowan looping is believed to be the operating strengthening mechanism.

For the shearing mechanism, three main factors contributing to the increase of yield strength are coherency strengthening ($\Delta\sigma_{coherency}$), order strengthening ($\Delta\sigma_{order}$) and modulus mismatch strengthening ($\Delta\sigma_{modulus}$) [47].

First, the stress field associated with the misfit strain between the coherent precipitates and matrix interacts with the stress field of dislocations giving rise to coherency strengthening expressed as [48]

$$\Delta\sigma_{coherency} = M\chi(\varepsilon G)^{\frac{3}{2}}(\frac{rfb}{\Gamma})^{\frac{1}{2}}$$

(4)

where M=2.9 is the Taylor factor for BCC metals in tension; χ is a constant with a value of 2.6; G=77 GPa is the shear modulus of the ferrite matrix [49], r is the mean radius of the precipitates, b≈0.25 nm is the magnitude of the Burgers vector in the ferrite matrix, f is the volume fraction of the precipitates, $\Gamma \approx Gb^2/2$ is the dislocation line tension, ε is the lattice mismatch parameter defined as $\varepsilon = \left|\frac{a_p - a_m}{a_m}\right|\left[\frac{1+2G(1-2v_p)}{G_p(1+v_p)}\right]$ in which a_p=0.289 nm and a_m=0.286 nm are the lattice parameters of the β-NiAl precipitate and ferrite matrix, G_p=73 GPa and v_p=0.31 are the shear modulus and Poisson's ratio of the β-NiAl precipitate [50].

Second, when dislocations cut through the ordered β-NiAl precipitates, anti-phase boundaries (APBs) with specific energies are created leading to the order strengthening effect. Adopting a simple yet common assumption that the fine precipitates are cut by weakly coupled pairs of dislocations with the trailing one remaining straight whilst the leading one bows out, the order strengthening ($\Delta\sigma_{order}$) can be described as [48]:

$$\Delta\sigma_{order} = 0.81M\frac{\gamma_{APB}}{2b}[(\frac{3\pi f}{8})^{\frac{1}{2}} - f] \tag{5}$$

where γ_{APB} is the APB energy of the precipitate phase and other parameters are the same as those defined in Equations (4). The reported values of 1/2<111>{110} APB energy in single crystal NiAl showed wide variation, ranging from 200±40 mJ·m^{-2} [51] to 800±40 mJ·m^{-2} [52]. A more recent review by Noebe *et al.* [50] compared experimental work by weak beam TEM with theoretical calculations and concluded that APB energy in NiAl should have a value towards the higher end of this range with γ_{APB} of 1/2<111>{110} of at least 500 mJ·m^{-2}. The value of $\gamma_{APB} = $ 500 mJ·m^{-2} was also used in recent work as the APB energy of β-NiAl precipitates in steels [19, 46]. Therefore, the same value is adopted in the current study.

Third, as a dislocation moves from the matrix into a particle of different shear modulus, there is a change in dislocation energy giving rise to the modulus mismatch strengthening effect. There are a number of theoretical approaches proposed by different researchers. For example, the Russell-Brown [53] model has been used in recent studies [19, 54] to calculate $\Delta\sigma_{modulus}$ caused by Cu and β-NiAl precipitates in steels for its simplicity. However, this approach requires the estimates of mean particle interspacing L which may be subject to considerable error; possibly as much as 50 % according to Russell and Brown [53]. Conversely, the Melander-Persson [55] approach, which have been used to quantify $\Delta\sigma_{modulus}$ in precipitate strengthened aluminium alloys [47, 56], does not require the estimated value of L according to the following expression:

$$\Delta\sigma_{modulus} = 0.0055M(\Delta G)^{\frac{3}{2}}(\frac{f}{\Gamma})^{\frac{1}{2}}b(\frac{r}{b})^{\frac{3m}{2}-1} \tag{6}$$

where m=0.85 is a constant, ΔG is difference of the shear modulus between the ferrite matrix (*G*=77 GPa) and the β–NiAl (*G*$_p$=73 GPa), and other parameters are the same as defined in Equation (4). Considering the difficulty to accurately determine the mean interspacing between β-NiAl precipitates, it is believed that the Melander-Persson approach is more appropriate to estimate the modulus strengthening effect of β–NiAl.

Finally, for the Orowan looping mechanism, the yield strength increment ($\Delta\sigma_{Orowan}$) is given as [56]:

$$\Delta\sigma_{Orowan} = M \frac{0.4Gb}{\pi\sqrt{1-v}} \frac{1}{L} \ln(\frac{2r_s}{b}) \tag{7}$$

where $v \approx 0.3$ is the Poisson's ratio of the matrix and L is mean inter-precipitate distance, $r_s = (2/3)^{1/2}r$ is the mean radius in the glide plane, other parameters are the same as the ones in Equation (5).

Using Equations (4) to (7) and the spatial distribution characteristics of the precipitates listed in Table 4, the contributions to yield strength from β-NiAl and secondary Laves phase precipitates after HT1 and HT3 by various strengthening mechanisms can be estimated and listed in Table 8.

Table 8 Estimated contributions to yield strength from different precipitates after HT1 and HT3 by various strengthening mechanisms, all unit in MPa.

Heat Treatment	β-NiAl				Laves phase	Total
	$\Delta\sigma_{coherency}$	$\Delta\sigma_{order}$	$\Delta\sigma_{modulus}$	Sub total	$\Delta\sigma_{Orowan}$	
HT1	53	603	46	702	199	901
HT3	52	641	53	746	201	947

The strengthening provided by β-NiAl precipitates to YS is in the range of 700 MPa, which is about 3.5 times of the contribution (~200 MPa) from the Laves phase. The different spatial distribution of precipitation phases due to the different heat treatment conditions between HT1 and HT3 contributed to a total difference of ~46 MPa. This is about half of the observed 93 MPa (see Table 3) difference in YS. In general, the effect of different heat treatment used in this study on YS of the maraging steel is very limited. However, the heat treatment effect on tensile ductility and fracture behaviour is significant (see Table 3 and Figure 3). This effect is believed to be predominately the result of the different volume fractions of β-NiAl precipitates after HT1 (~12%) and HT3 (~16%). Recent studies [31, 32, 57] on a series of β-NiAl strengthened ferritic steels showed that the two major factors governing the ductility are (i) the volume fraction of β-NiAl and (ii) the Al content in the α-Fe matrix. It has been shown that when the volume fraction of β-NiAl decreased from 13.6 % to 7.3 %, the bending ductility increased dramatically from 1.5 % to 5 % [31] accompanied by a possible change of the fracture mode from distinctive brittle cleavage to a mixture with substantial ductile fractures [32]. These behaviours are very similar to the observed differences between HT1 and HT3 in this study. As the Al content in the matrix

after the ageing heat treatment is very similar between HT1 and HT3 (see Table 5), it is not considered as a major contribution factor to the observed difference in tensile ductility.

The outstanding heat resistance performance of this steel achieved by the unique combination of β-NiAl and Laves phase precipitates is clearly demonstrated in Figure 5. In comparison, heat resistant steels strengthened mainly by β-NiAl phase, such as the well reported 'FBB-8' family [18, 58, 59], had a YS of about 600 MPa at 500 °C [60], which is well below the applied stress (700 MPa) in the creep tests at the same temperature in the current study. Similarly, 15Cr ferritic heat resistant steels that are primarily strengthened by Laves phase showed an UTS of ~600 MPa at 500 °C [61]. In contrast, the YS and UTS of the maraging steel in this study are in the range of 1100 MPa and 1400 MPa, respectively.

The impact of different heat treatments on creep performance of this steel is also significant as shown in Figure 5. According to Abe [43], for 9Cr (wt.%) tempered martensitic steels, the transient creep, i.e. the linear decrease of creep rate during the early stage in creep testing, is basically the consequence of the movement and annihilation of dislocations; meanwhile, the onset of accelerated creep is closely associated with the migration of boundaries, i.e. the microstructure instability. For HT1 and HT2, the onset of accelerated creep is very early, only 10-20 hours into creep testing; whilst for HT3 the transient creep lasted to ~1,000 hours before the onset of accelerated creep. As extensive fine and continuous Laves phase precipitates are found along lath boundaries after ageing (e.g. see Figure 13), the lath boundaries were essentially immobilised. Instead, in the maraging steel of this study, cavitation is believed to be the dominant creep failure mechanisms. Indeed, TEM examination of fractured creep samples after both HT1 and HT3 found extensive cavities in the microstructure particularly at Y-junction of lath boundaries, triple junction of PAGBs and most importantly between primarily Laves phase particles and matrix [62]. On the other hand, no apparent difference was observed between HT1 and HT3 after interrupted creep testing to 0.5% creep strain [62]. These observations suggest that the large primary Laves phase particles formed during austenisation at lower temperatures are detrimental to creep rupture life in this maraging steel, especially those found on PAGB. This is also supported by the distinctly different creep fracture surfaces shown in Figure 6, with HT1 showing characteristic intergranular fracture whilst HT3 exhibiting predominantly microvoid coalescence.

5. Conclusions

A novel ultra-high strength maraging steel was developed utilising nanostructured intermetallic precipitates of β-NiAl and Laves phase. With different heat treatment, this steel showed a remarkable combination of mechanical properties: yield strength of >1800 MPa, ultimate tensile strength of ~ 2000 MPa, tensile ductility up to ~8% at room temperature and creep rupture life > 2,000 hours under 700 MPa stress at 500 °C. By characterising the microstructures at different length scales using optical metallography, SEM/EBSD, TEM and atom probe tomography, insights were obtained to understand better the effect of heat treatment conditions on the microstructure development in this steel to achieve more balanced strength, ductility and creep life.

The following conclusions can be made:

(i)   Large primary Mo, W and Cr rich Laves phase precipitates were formed at PAGBs and planner defects within PAGs during austenisation at temperatures below the Laves phase solvus. The primary Laves phase precipitates were believed to be detrimental to the creep rupture life of this steel.

(ii)   The 20 °C difference between ageing at lower temperature of 540 °C and higher temperature of 560 °C had negligible effect on the secondary Laves phase precipitates in terms of both chemical compositions and spatial distribution characteristics.

(iii)   Whilst the chemical composition of the β-NiAl precipitates was not strongly affected by the different ageing temperatures, its spatial distribution characteristics were significantly affected. Ageing at the lower temperature of 540 °C produced much smaller β-NiAl precipitates with higher number density and volume fraction compared to ageing at 560 °C for the same duration of 5 hours.

(iv)   The main strengthening mechanism provided by secondary Laves phase precipitates is Orowan looping whilst β-NiAl precipitates provide strengthening by particle shearing. The contribution to yield strength from β-NiAl precipitates is estimated to be ~3.5 times of that from the secondary Laves phase ones. However, the secondary Laves phase precipitates on martensitic lath boundaries are believed to be important for the creep life by degreasing the mobility of these boundaries.

(v)   For complex alloying system in this novel steel, careful design of heat treatment aided by computational thermodynamics method is still required to achieve balanced mechanical properties that can meet stringent service requirements in aerospace propulsion system.

Acknowledgements

References

[1] J.C. Williams, E.A. Starke Jr, Progress in structural materials for aerospace systems, Acta Mater. 51(19) (2003) 5775-5799.

[2] P. Liu, A.H. Stigenberg, J.O. Nilsson, Quasicrystalline and crystalline precipitation during isothermal tempering in a 12Cr-9Ni-4Mo maraging stainless steel, Acta Metall. Mater. 43(7) (1995) 2881-2890.

[3] R. Tewari, S. Mazumder, I.S. Batra, G.K. Dey, S. Banerjee, Precipitation in 18 wt% Ni maraging steel of grade 350, Acta Mater. 48(5) (2000) 1187-1200.

[4] W.M. Garrison, Jr., Ultrahigh-strength steels for aerospace applications, JOM 42(5) (1990) 20-24.

[5] W. Sha, Z. Guo, Maraging steels : modelling of microstructure, properties and applications, Woodhead Publishing ; CRC Press, Oxford; Boca Raton, Fla., 2009.

[6] E.V. Pereloma, A. Shekhter, M.K. Miller, S.P. Ringer, Ageing behaviour of an Fe–20Ni–1.8Mn–1.6Ti–0.59Al (wt%) maraging alloy: clustering, precipitation and hardening, Acta Mater. 52(19) (2004) 5589-5602.

[7] U.K. Viswanathan, G.K. Dey, V. Sethumadhavan, Effects of austenite reversion during overageing on the mechanical properties of 18 Ni (350) maraging steel, Materials Science and Engineering: A 398(1–2) (2005) 367-372.

[8] T. Simm, L. Sun, S. McAdam, P. Hill, M. Rawson, K. Perkins, The Influence of Lath, Block and Prior Austenite Grain (PAG) Size on the Tensile, Creep and Fatigue Properties of Novel Maraging Steel, Materials 10(7) (2017) 730.

[9] T.H. Simm, L. Sun, D.R. Galvin, E.P. Gilbert, D. Alba Venero, Y. Li, T.L. Martin, P.A.J. Bagot, M.P. Moody, P. Hill, H.K.D.H. Bhadeshia, S. Birosca, M.J. Rawson, K.M. Perkins, A SANS and APT study of precipitate evolution and strengthening in a maraging steel, Materials Science and Engineering: A 702 (2017) 414-424.

[10] H. Cui, F. Sun, K. Chen, L. Zhang, R. Wan, A. Shan, J. Wu, Precipitation behavior of Laves phase in 10%Cr steel X12CrMoWVNbN10-1-1 during short-term creep exposure, Materials Science and Engineering: A 527(29–30) (2010) 7505-7509.

[11] F. Abe, Effect of fine precipitation and subsequent coarsening of Fe2W laves phase on the creep deformation behavior of tempered martensitic 9Cr-W steels, Metall. Mater. Trans. A 36(2) (2005) 321-332.

[12] J. Hald, Microstructure and long-term creep properties of 9–12% Cr steels, International Journal of Pressure Vessels and Piping 85(1–2) (2008) 30-37.

[13] D.B. Miracle, Overview No. 104 The physical and mechanical properties of NiAl, Acta Metall. Mater. 41(3) (1993) 649-684.

[14] Z. Guo, W. Sha, D. Vaumousse, Microstructural evolution in a PH13-8 stainless steel after ageing, Acta Mater. 51(1) (2003) 101-116.

[15] H. Leitner, R. Schnitzer, M. Schober, S. Zinner, Precipitate modification in PH13-8 Mo type maraging steel, Acta Mater. 59(12) (2011) 5012-5022.

[16] M.A. Rhoads, E.L. Raymond, W.M. Garrison, High strength, high fatigue structural steel 1995.

[17] Z. Sun, C.H. Liebscher, S. Huang, Z. Teng, G. Song, G. Wang, M. Asta, M. Rawlings, M.E. Fine, P.K. Liaw, New design aspects of creep-resistant NiAl-strengthened ferritic alloys, Scripta Mater. 68(6) (2013) 384-388.

[18] Z.K. Teng, M.K. Miller, G. Ghosh, C.T. Liu, S. Huang, K.F. Russell, M.E. Fine, P.K. Liaw, Characterization of nanoscale NiAl-type precipitates in a ferritic steel by electron microscopy and atom probe tomography, Scripta Mater. 63(1) (2010) 61-64.

[19] Z.B. Jiao, J.H. Luan, Z.W. Zhang, M.K. Miller, C.T. Liu, High-strength steels hardened mainly by nanoscale NiAl precipitates, Scripta Mater. 87 (2014) 45-48.

[20] D.H. Ping, M. Ohnuma, Y. Hirakawa, Y. Kadoya, K. Hono, Microstructural evolution in 13Cr–8Ni–2.5Mo–2Al martensitic precipitation-hardened stainless steel, Materials Science and Engineering: A 394(1–2) (2005) 285-295.

[21] J. Janovec, B. Richarz, H.J. Grabke, Some aspects of intermetallic phase precipitation in a 12% Cr-steel, Scripta Metall. Mater. 33(2) (1995) 295-300.

[22] L. Sun, M.J. Thomas, B.P. Wynne, E.J. Palmiere, K.P. Mingard, B. Roebuck, Mapping microstructure inhomogeneity using electron backscatter diffraction in 316L stainless steel subjected to hot plane strain compression tests, Mater. Sci. Technol. 26(12) (2010) 1477-1486.

[23] B. Gault, Atom probe microscopy, Springer, New York, 2012.

[24] M.K. Miller, K.F. Russell, K. Thompson, R. Alvis, D.J. Larson, Review of atom probe FIB-Based specimen preparation methods, Microsc. Microanal. 13(6) (2007) 428-436.

[25] K. Thompson, B. Gorman, D. Larson, B.v. Leer, L. Hong, Minimization of Ga Induced FIB Damage Using Low Energy Clean-up, Microsc. Microanal. 12(SupplementS02) (2006) 1736-1737.

[26] R.H. Dauskardt, F. Haubensak, R.O. Ritchie, On the interpretation of the fractal character of fracture surfaces, Acta Metall. Mater. 38(2) (1990) 143-159.

[27] S. Morito, X. Huang, T. Furuhara, T. Maki, N. Hansen, The morphology and crystallography of lath martensite in alloy steels, Acta Mater. 54(19) (2006) 5323-5331.

[28] H. Kitahara, R. Ueji, N. Tsuji, Y. Minamino, Crystallographic features of lath martensite in low-carbon steel, Acta Mater. 54(5) (2006) 1279-1288.

[29] T. Juuti, L. Rovatti, A. Mäkelä, L.P. Karjalainen, D. Porter, Influence of long heat treatments on the laves phase nucleation in a type 444 ferritic stainless steel, J. Alloys Compd. 616(0) (2014) 250-256.

[30] R.P. Kolli, D.N. Seidman, Comparison of Compositional and Morphological Atom-Probe Tomography Analyses for a Multicomponent Fe-Cu Steel, Microsc. Microanal. 13(04) (2007) 272-284.

[31] Z.K. Teng, C.T. Liu, M.K. Miller, G. Ghosh, E.A. Kenik, S. Huang, P.K. Liaw, Room temperature ductility of NiAl-strengthened ferritic steels: Effects of precipitate microstructure, Materials Science and Engineering: A 541 (2012) 22-27.

[32] Z.K. Teng, C.T. Liu, G. Ghosh, P.K. Liaw, M.E. Fine, Effects of Al on the microstructure and ductility of NiAl-strengthened ferritic steels at room temperature, Intermetallics 18(8) (2010) 1437-1443.

[33] T.L. Martin, A. Radecka, L. Sun, T. Simm, D. Dye, K. Perkins, B. Gault, M.P. Moody, P.A.J. Bagot, Insights into microstructural interfaces in aerospace alloys characterised by atom probe tomography, Mater. Sci. Technol. 32(3) (2016) 232-241.

[34] A. Kipelova, A. Belyakov, R. Kaibyshev, Laves phase evolution in a modified P911 heat resistant steel during creep at 923 K, Materials Science and Engineering: A 532 (2012) 71-77.

[35] S. Liu, Precipitation Processes in Fe-Cr-5W Ternary Alloys, J. Jpn. Inst. Met. 52(10) (1988) 927-934.

[36] K. Yamamoto, Y. Kimura, Y. Mishima, Effect of matrix microstructure on precipitation of Laves phase in Fe–10Cr–1.4W(–Co) alloys, Intermetallics 14(5) (2006) 515-520.

[37] L.V. Tarasenko, V.I. Titov, Intermetallic R-phase in maraging steels of the Fe-Cr-Ni-Co-Mo system, Met. Sci. Heat Treat. 48(7-8) (2006) 374-378.

[38] A. Aghajani, F. Richter, C. Somsen, S.G. Fries, I. Steinbach, G. Eggeler, On the formation and growth of Mo-rich Laves phase particles during long-term creep of a 12% chromium tempered martensite ferritic steel, Scripta Mater. 61(11) (2009) 1068-1071.

[39] A. Aghajani, C. Somsen, G. Eggeler, On the effect of long-term creep on the microstructure of a 12% chromium tempered martensite ferritic steel, Acta Mater. 57(17) (2009) 5093-5106.

[40] Y. Hosoi, N. Wade, S. Kunimitsu, T. Urita, Precipitation behavior of laves phase and its effect on toughness of 9Cr-2Mo Ferritic-martensitic steel, J. Nucl. Mater. 141 (1986) 461-467.

[41] D. Delagnes, F. Pettinari-Sturmel, M.H. Mathon, R. Danoix, F. Danoix, C. Bellot, P. Lamesle, A. Grellier, Cementite-free martensitic steels: A new route to develop high strength/high toughness grades by modifying the conventional precipitation sequence during tempering, Acta Mater. 60(16) (2012) 5877-5888.

[42] S.D. Erlach, H. Leitner, M. Bischof, H. Clemens, F. Danoix, D. Lemarchand, I. Siller, Comparison of NiAl precipitation in a medium carbon secondary hardening steel and C-free PH13-8 maraging steel, Materials Science and Engineering: A 429(1–2) (2006) 96-106.

[43] F. Abe, Precipitate design for creep strengthening of 9% Cr tempered martensitic steel for ultra-supercritical power plants, Science and Technology of Advanced Materials 9(1) (2008) 013002.

[44] T. Gladman, Precipitation hardening in metals, Mater. Sci. Technol. 15(1) (1999) 30-36.

[45] L. Proville, B. Bakó, Dislocation depinning from ordered nanophases in a model fcc crystal: From cutting mechanism to Orowan looping, Acta Mater. 58(17) (2010) 5565-5571.

[46] E. Povoden-Karadeniz, E. Kozeschnik, Simulation of Precipitation Kinetics and Precipitation Strengthening of B2-precipitates in Martensitic PH 13–8 Mo Steel, ISIJ Int. 52(4) (2012) 610-615.

[47] D.N. Seidman, E.A. Marquis, D.C. Dunand, Precipitation strengthening at ambient and elevated temperatures of heat-treatable Al(Sc) alloys, Acta Mater. 50(16) (2002) 4021-4035.

[48] A.J. Ardell, Precipitation hardening, Metall. Trans. A 16(12) (1985) 2131-2165.

[49] A. Deschamps, M. Militzer, W.J. Poole, Precipitation Kinetics and Strengthening of a Fe–0.8wt%Cu Alloy, ISIJ Int. 41(2) (2001) 196-205.

[50] R.D. Noebe, R.R. Bowman, M.V. Nathal, Physical and mechanical properties of the B2 compound NiAl, Int. Mater. Rev. 38(4) (1993) 193-232.

[51] R.G. Campany, M.H. Loretto, R.E. Smallman, The determination of the 1/2<lll> {110} antiphase boundary energy of NiAl, J. Microsc. 98(2) (1973) 174-179.

[52] C.L. Fu, M.H. Yoo, Deformation behavior of B2 type aluminides: FeAl and NiAl, Acta Metall. Mater. 40(4) (1992) 703-711.

[53] K.C. Russell, L.M. Brown, A dispersion strengthening model based on differing elastic moduli applied to the iron-copper system, Acta Metall. 20(7) (1972) 969-974.

[54] Z.B. Jiao, J.H. Luan, Z.W. Zhang, M.K. Miller, W.B. Ma, C.T. Liu, Synergistic effects of Cu and Ni on nanoscale precipitation and mechanical properties of high-strength steels, Acta Mater. 61(16) (2013) 5996-6005.

[55] A. Melander, P.Å. Persson, The strength of a precipitation hardened AlZnMg alloy, Acta Metall. 26(2) (1978) 267-278.

[56] K. Ma, H. Wen, T. Hu, T.D. Topping, D. Isheim, D.N. Seidman, E.J. Lavernia, J.M. Schoenung, Mechanical behavior and strengthening mechanisms in ultrafine grain precipitation-strengthened aluminum alloy, Acta Mater. 62 (2014) 141-155.

[57] Z.K. Teng, F. Zhang, M.K. Miller, C.T. Liu, S. Huang, Y.T. Chou, R.H. Tien, Y.A. Chang, P.K. Liaw, New NiAl-strengthened ferritic steels with balanced creep resistance and ductility designed by coupling thermodynamic calculations with focused experiments, Intermetallics 29 (2012) 110-115.

[58] Z.B. Jiao, J.H. Luan, M.K. Miller, Y.W. Chung, C.T. Liu, Co-precipitation of nanoscale particles in steels with ultra-high strength for a new era, Mater. Today 20(3) (2017) 142-154.

[59] G. Song, Z. Sun, L. Li, X. Xu, M. Rawlings, C.H. Liebscher, B. Clausen, J. Poplawsky, D.N. Leonard, S. Huang, Z. Teng, C.T. Liu, M.D. Asta, Y. Gao, D.C. Dunand, G. Ghosh, M. Chen, M.E. Fine, P.K. Liaw, Ferritic Alloys with Extreme Creep Resistance via Coherent Hierarchical Precipitates, Scientific Reports 5 (2015) 16327.

[60] S. Huang, Y. Gao, K. An, L. Zheng, W. Wu, Z. Teng, P.K. Liaw, Deformation mechanisms in a precipitation-strengthened ferritic superalloy revealed by in situ neutron diffraction studies at elevated temperatures, Acta Mater. 83 (2015) 137-148.

[61] M. Shibuya, Y. Toda, K. Sawada, H. Kushima, K. Kimura, Effect of nickel and cobalt addition on the precipitation-strength of 15Cr ferritic steels, Materials Science and Engineering: A 528(16) (2011) 5387-5393.

[62] L. Sun, S.W. Ooi, Unpublished Work, University of Cambridge, Cambridge, 2016.